

Model reduction for fluids using frequential snapshots

G. Dergham,^{1,2} D. Sipp,² J.-C. Robinet,¹ and A. Barbagallo^{2,3}

¹*DynFluid Laboratory, Arts et Métiers ParisTech, 151 Bd de l'Hôpital, 75013 Paris, France*

²*ONERA, Fundamental and Experimental Aerodynamics Department, 8 rue des vertugadins, 92190 Meudon, France*

³*LadHyX Laboratory, École Polytechnique, 91128 Palaiseau, France*

(Received 15 July 2010; accepted 24 February 2011; published online 10 June 2011)

This paper deals with model reduction of high-order linear systems. An alternative method to approximate proper orthogonal decomposition (POD) and balanced truncation is exposed in this paper within the framework of the incompressible Navier-Stokes equations. The method of snapshots used to obtain low-rank approximations of the system controllability and observability Gramians is carried out in the frequency domain. Model reduction is thus performed using flow states that are long-time harmonic responses of the flow to given forcings, we call them frequential snapshots. In contrast with the recent works using time-stepping approach, restricted to stable systems, this one can always be computed for systems without marginal modes while it reduces to the same procedure for stable systems. We show that this method is efficient to perform POD and balanced proper orthogonal decomposition reduced-order models in both globally stable and unstable flows through two numerical examples: the flow over a backward-facing step and the flow over a square cavity. The first one is a globally stable flow exhibiting strong transient growths as a typical noise amplifier system while the second is a globally unstable flow representative of an oscillator system. In both cases, it is shown that the frequency-based snapshot method yields reduced-order models that efficiently capture the input-output behavior of the system. In particular, regarding the unstable cavity flow, our resulting unstable reduced-order models possess the same unstable global modes and stable transfer functions as those of the full system. © 2011 American Institute of Physics. [doi:10.1063/1.3590732]

I. INTRODUCTION

During the last decade, linear state space flow control has become a new and promising research subject.^{1,2} Originally introduced for flows governed by linear instability mechanisms,^{3,4} it brought control theoretical tools,^{5,6} such as optimal control, within the reach of the fluid mechanics community. Optimal flow control obviously displays attractive features. One may refer to previous works such as the control of a transitional boundary layer,^{7,8} a transitional channel flow,⁹ or also turbulent channel flows.^{10,11} Yet, as soon as complex or more realistic flows are considered, the direct application of many optimal flow control tools is no more computationally tractable. One may then resort to a modeling of the dynamics by reduced-order models (ROMs) to alleviate this problem. In this context, modeling the dynamics between some particular inputs, such as the actuators, and some particular outputs, such as the sensors, may be sufficient to perform effective optimal flow control. For instance, let us mention the application of Linear Quadratic Gaussian (LQG) closed-loop flow control^{12–15} to more complex flows. The goal of this paper is to explore an alternative way of performing such ROMs in the context of transitional separated flows.

The proper orthogonal decomposition (POD) method has been used extensively for reduced-order modeling of fluid mechanics problems. It was proposed by Lumley¹⁶ as an unbiased technique for identifying the most energetic patterns (or structures) in a flow. In particular, POD has been

shown to yield a valuable analysis tool to discriminate coherent structures in turbulent flows.^{17,18} Thus, POD modes stand for natural candidates to design ROMs. This may be achieved by projecting the original equations (either linear or not) onto the POD modes. Such a reduced modeling of the Navier-Stokes equations was first performed by Aubry *et al.*¹⁹ Noticeably, a time-space deterministic version of the POD has been introduced by Aubry *et al.*²⁰ as a systematic tool for complex system analysis. This latter consists of a bi-orthogonal decomposition into spatial orthogonal modes (similar to the POD modes) and temporal orthogonal modes (standing for the deterministic time coefficients of the modes). Since then, POD model reduction has spawned a substantial body of literature on low-dimensional models for flows.^{21–23} Recently, POD based ROMs have also been incorporated into flow control strategies for the flow around a cylinder^{24–26} or the flow over an open cavity.²⁷ Although this model reduction technique is tractable for very large data sets and applicable to complex flows, POD modes may not be the best structures for describing the dynamics, even in a linearized case. Indeed, the truncated low-energy features of a flow may contribute to a significant part of the global dynamics, as in the typical example of acoustic modes in cavity oscillations.²⁸

Within the context of model reduction, both the controllability, i.e., the ability of the applied forcing to reach flow states, and observability, i.e., the ability of flow states to register at the sensor locations, are equally important. An expansion basis that balances these two concepts was

introduced more than two decades ago for stable, linear input-output systems by Moore.²⁹ Introducing the controllability and observability Gramians (which yield a measure of controllability and observability of the system), it is shown²⁹ that such a basis can be computed as the eigenvectors of the product of these two Gramians. Model reduction is then performed by considering a basis where the states that respond most strongly to inputs (most controllable states) are also states that have the most influence on the outputs (most observable states). This powerful technique, commonly applied in control theory, is known as balanced truncation and constitutes a quasi-optimal basis in terms of modeling the input-output dynamics. Further development of the method extended its range to nonlinear control problems, see Scherpen³⁰ and Lall *et al.*³¹ An optimal and accurate algorithm for the calculation of this basis has been found by Laub *et al.*³² and has been used on some fluid problems of small size³³ but its associated computational effort is rather high for systems of moderate size and quickly becomes unaffordable for systems of large size and realistic complexity (about 5000 states or more).

However, recent developments by Willcox and Peraire³⁴ and Rowley³⁵ combining computational methodology from POD modes with a balancing procedure have overcome this difficulty and have brought the model reduction of large-scale control problems within reach of current computational technology. It was shown that the Gramians can be approximated using two series of snapshots resulting from two different numerical simulations and that the algorithm of Laub *et al.*³² can be generalized to take into account these approximate Gramians. This new method is referred as balanced proper orthogonal decomposition (BPOD) due to the use of flow snapshots and the connection to POD established by Rowley.³⁵ This new technique has been applied to several linearized stable flows: the case of a channel flow,^{36,37} a one-dimensional model equation mimicking an open flow,³⁸ and a boundary-layer flow.¹³

Regarding the reduction of linearized unstable systems, the original method of Moore²⁹ is no longer applicable. To overcome this limitation, an extension was proposed by Zhou *et al.*³⁹ by introducing frequency-domain definitions of controllability and observability Gramians. In contrast to Gramians defined in the literature for stable systems, these Gramians can always be computed for systems without marginal modes and they reduce to the standard controllability and observability Gramians when the systems are stable.^{40,41} The model reduction procedure of Zhou *et al.*³⁹ essentially decouples the dynamics of the flow on the stable and unstable subspaces and then truncates the relatively uncontrollable and unobservable modes of each of the two subspaces. Following this idea, Ahuja and Rowley^{14,42} performed a model reduction of the unstable linearized flow over an inclined flat plate by partitioning the system behavior into stable and unstable dynamics. In this case, the stable subspace was modeled by the standard BPOD algorithm of Rowley,³⁵ while the unstable dynamics were treated similarly to the work of Åkervik *et al.*¹² by a projection onto global eigenmodes. The same partitioning has also been carried out by Barbagallo *et al.*¹⁵ in the case of the unstable dynamics over a

square cavity flow. In both studies, the unstable global modes are first computed via a shift-invert Arnoldi technique, and then used to project the series of snapshots required by the BPOD process onto the stable subspace.

In this paper, we are interested in another method for the balancing and reduction of possibly unstable systems. It consists in using the frequency-domain definitions of the controllability and observability Gramians proposed by Zhou *et al.*³⁹ and an approximation of these Gramians with frequential snapshots. This way, the Gramians are no longer approximated by using two series of snapshots arising from time-stepping simulations but rather by using flow state responses to harmonic forcings. These flow states involved in the process are called frequential snapshots throughout this work due to their natural link with the current time-based snapshot method. The idea to use frequential expressions of the Gramians and to compute frequential snapshots to perform reduced-order models has already been introduced by Willcox and Peraire,³⁴ although it has never been carried out. The goal of this paper is to show that the use of these frequential snapshots is able to build efficient reduced order models for linearized and possibly unstable fluid systems in a global framework. This issue is studied through two examples: a globally stable but convectively unstable flow over a rounded backward-facing step and a globally unstable flow over a square cavity. In both cases, a single actuator (input) and a single sensor (output) are placed near separation and reattachment, respectively. The approximate balanced truncation procedure is then derived considering this input and output using the snapshot method in the frequential framework. At the same time, the POD modes constructed from an impulse released from the input, i.e., the most controllable modes, are also considered and computed through the same frequential snapshots. Both BPOD and POD reduced-order models are eventually evaluated by comparing their impulse and frequency responses to that of their associated full system. In the case of the unstable flow over the square cavity, particular care is given to the reduction performance of the stable and unstable subspaces. Additionally, our results are compared to a previous study¹⁵ on the same flow configuration where partitioning of the two subspaces and separate reduction was performed. The main contributions of this work comprise (1) an illustration of the ability of harmonic flow states responses (frequential snapshots) to build efficient BPOD/POD reduced-order models and (2) a new algorithm to perform model reduction for unstable linear systems without partitioning the stable and unstable subspace and, thus, without computing any global eigenmodes.

The article proceeds along the following outline. In Sec. II, we first briefly describe the BPOD and POD model reduction procedure using frequential snapshots within the framework of the linearized Navier-Stokes equations with actuation and sensing. In particular, a comparison of the computational costs of the temporal and frequential domain based snapshot method is assessed. In Sec. III, we present numerical results of ROMs using the example of a globally stable flow over a backward-facing step. In Sec. IV, we investigate the case of a globally unstable flow over a square cavity and compare our ROMs performance with a previous

work on this configuration.¹⁵ The paper concludes with a brief discussion in Sec. V.

II. MODEL REDUCTION METHODOLOGY

A. Problem formulation

1. Governing equations

We consider the incompressible Navier-Stokes equations, with a small actuation and a sensing, governing the dynamics of the velocity \mathbf{u} and pressure p fields

$$\begin{cases} \partial_t \mathbf{u} + (\mathbf{u} \cdot \nabla) \mathbf{u} = -\nabla p + Re^{-1} \nabla^2 \mathbf{u} + \varepsilon \mathcal{B}c(t) \\ \nabla \cdot \mathbf{u} = 0 \\ m(t) = \mathcal{C} \mathbf{u} \end{cases} \quad (1)$$

where the only parameter reduces to the Reynolds number Re . The actuation is denoted by the term $\varepsilon \mathcal{B}c(t)$ corresponding to a momentum forcing. The parameter ε indicates that the forcing is small compared to the other terms of the equation and $c(t)$ is the temporal law of the actuation also referred to as the input of the problem. The quantity $m(t)$ measured by the sensor stands for the output of the system; it is expressed as the result of a measure operator \mathcal{C} applied on the velocity field \mathbf{u} . Note that we have assumed an actuation and sensing based on the velocity components only for simplicity. Considering this problem, we wished to design a reduced-order model able to capture the linear input-output dynamics of this system.

Before proceeding with model reduction, we first express the governing equations in a linear state-space form. To this end, a base flow (\mathbf{U}, P) to linearize about has to be determined. This is accomplished by setting the unsteady terms of Eqs. (1) to zero and solving the resulting nonlinear equations

$$\begin{cases} (\mathbf{U} \cdot \nabla) \mathbf{U} = -\nabla P + Re^{-1} \nabla^2 \mathbf{U} \\ \nabla \cdot \mathbf{U} = 0 \\ m_s = \mathcal{C} \mathbf{U} \end{cases} \quad (2)$$

where m_s stands for the measure of the base flow. The flow state can then be decomposed as the sum of the base flow and a small perturbation by $(\mathbf{u}, p) = (\mathbf{U}, P) + \varepsilon(\mathbf{u}', p')$. Similarly, the measure $m(t)$ can be decomposed as the sum of the steady part coming from the base flow and the small contribution from the perturbation as $m(t) = m_s + \varepsilon m'(t)$, where $m'(t) = \mathcal{C} \mathbf{u}'$. Substitution of these decompositions into Eqs. (1), neglecting the ε^2 term and omitting primes yields the linearized Navier-Stokes equations

$$\begin{cases} \partial_t \mathbf{u} + \mathbf{U} \cdot \nabla \mathbf{u} + \mathbf{u} \cdot \nabla \mathbf{U} = -\nabla p + Re^{-1} \nabla^2 \mathbf{u} + \mathcal{B}c(t) \\ \nabla \cdot \mathbf{u} = 0 \\ m(t) = \mathcal{C} \mathbf{u} \end{cases} \quad (3)$$

which govern the linear dynamics about the considered base flow. It is furthermore assumed that the amplitude of the perturbation remains weak compared to the base flow so that the validity of Eqs. (3) is guaranteed.

Using a numerical approach, one then proceeds by discretizing the problem on a mesh (ours is based on a finite element method described in the end of this section). If we write the discretized equations (3) in matrix form, we obtain

$$\begin{pmatrix} \mathbf{Q}_1 & 0 \\ 0 & 0 \end{pmatrix} \frac{d}{dt} \begin{pmatrix} \mathbf{X}_1 \\ \mathbf{X}_2 \end{pmatrix} = \begin{pmatrix} \mathbf{A}_1 & \mathbf{A}_2^* \\ \mathbf{A}_2 & 0 \end{pmatrix} \begin{pmatrix} \mathbf{X}_1 \\ \mathbf{X}_2 \end{pmatrix} + \begin{pmatrix} \mathbf{Q}_1 & 0 \\ 0 & 0 \end{pmatrix} \begin{pmatrix} \mathbf{B}_1 \\ 0 \end{pmatrix} c(t) \quad (4a)$$

$$m(t) = (\mathbf{C}_1 \quad 0) \begin{pmatrix} \mathbf{X}_1 \\ \mathbf{X}_2 \end{pmatrix} \quad (4b)$$

where \mathbf{X}_1 denotes the velocity fields and \mathbf{X}_2 stands for the corresponding pressure field. $(\mathbf{B}_1, 0)$ and $(\mathbf{C}_1, 0)$ denote the vectors of the discretized actuation \mathcal{B} and sensing \mathcal{C} operators, respectively. The linearized Navier-Stokes operator has been decomposed so that \mathbf{A}_1 stands for convection and diffusion while \mathbf{A}_2 and \mathbf{A}_2^* are the parts relative to incompressibility and pressure effect respectively, the superscript $*$ denoting the transconjugate. For the design of reduced-order models, we need to reformulate the above equations into a standard state-space form. This is achieved by restricting the system state to its divergence-free velocity field. A few calculations exposed in Appendix A demonstrate that Eqs. (4) can be formulated as the following standard linear input-output system

$$\frac{d\mathbf{X}_1}{dt} = \mathbf{A} \mathbf{X}_1 + \mathbf{B} c(t) \quad (5a)$$

$$m(t) = \mathbf{C} \mathbf{X}_1 \quad (5b)$$

where we have introduced $\mathbf{A} = \mathbf{P}_1 \mathbf{A}_1$, $\mathbf{B} = \mathbf{P}_1 \mathbf{Q}_1 \mathbf{B}_1$, and $\mathbf{C} = \mathbf{C}_1$, so that the projection matrix onto the divergence-free space reduces to $\mathbf{P}_1 \mathbf{Q}_1$. The dimension of the full system is called hereafter n_1 and denotes the number of degrees of freedom in Eq. (5) or alternatively the size of the discretized state velocity vector \mathbf{X}_1 . Once defined, our linear input-output state space system has to be associated with scalar products for the input, the output and the state space. Since the input and output are scalars, their associated inner product are naturally chosen as the standard Hermitian product so that their associated energy are, respectively, $|c|^2$ and $|m|^2$. As mentioned in the work of Ilak and Rowley,³⁷ the choice of inner product on the state space does not intervene in balanced truncation, although it does for POD. We choose the inner product \mathbf{Q}_1 that takes into account the numerical discretization by adding a weight matrix to the standard inner product. Its associated energy is $\mathbf{X}_1^* \mathbf{Q}_1 \mathbf{X}_1$, i.e., the kinetic energy of the perturbation. This choice is thus intuitively appealing, since POD will capture the true energy of the perturbations.

As recognized in existing literature,^{6,38,41} the input-output behavior is the critical quantity that has to be carefully taken into consideration within the framework of linear input-output system dynamics and more particularly in control theory. Mathematically, the relevant quantities to assess this performance are the impulse response and/or the transfer

function. As a result, these are the criteria considered in the following sections to quantify the performance of the ROMs.

2. Model reduction phenomenology

Before proceeding with a precise and more technical description of the model reduction procedure, we briefly introduce its concept here. For an easier physical interpretation of the procedure, we first assume that the fluid system is linearly stable; the case of unstable systems is discussed afterwards.

The actuator (input) excites the flow dynamics while the sensor yields a measure corresponding to the output. The present model reduction procedure consists in projecting the original Eqs. (5) onto a low number of flow structures. If we denote the projection basis by the matrix T_1 and its bi-orthogonal set by S_1 , then the Petrov-Galerkin projection of the original system provided by Eqs. (5) leads to the following reduced system:

$$\frac{dX_{1r}}{dt} = A_r X_{1r} + B_r c(t) \quad (6a)$$

$$m_r(t) = C_r X_{1r} \quad (6b)$$

which governs the dynamics of the reduced output signal $m_r(t)$ and the reduced state X_{1r} is such that $X_1 = T_1 X_{1r}$ and $X_{1r} = S_1^* Q_1 X_1$. We have also introduced in the above equations the reduced dynamical operator, actuation, and sensing denoted by A_r , B_r , and C_r , respectively. They are given by

$$A_r = S_1^* Q_1 A T_1, \quad B_r = S_1^* Q_1 B, \quad C_r = C T_1. \quad (7)$$

The performance of such ROMs is then assessed by comparing their input-output behavior to the original one. The choice of the projection basis is obviously of primary importance if one plans to design efficient ROMs. For stable linear systems, Moore²⁹ showed that their controllability and observability stand for critical quantities. By definition, a flow structure is said controllable if it may be forced by a small amount of energy from the input. Additionally, a flow structure is said observable if its dynamics yield a high energy contribution to the output. In this context, the two candidates examined here to project the dynamics are (1) the most controllable modes, denoted as POD modes, and (2) the set of equally (and most) controllable and observable modes, known as balanced modes.

Due to the linear nature of the equations, any harmonic excitation will lead to a harmonic flow response and, consequently, to a harmonic measurement. It is thus natural to resort to a frequency framework when dealing with such systems. Incidentally, the particularity of our work is the introduction of harmonic flow states meant to design efficient ROMs. Let us first describe the procedure to design the POD modes. We consider harmonic excitations from the input so as to get harmonic flow responses. By covering a sufficiently wide frequency range, we expect to capture the most energetic responses from all possible harmonic forcings. Next, based on these harmonic responses, we compute the set of most controllable modes on that frequency range. The result-

ing so-called POD modes are thus conceptually designed to optimally capture the energy triggered by the input on the particular frequency interval of interest. Now, regarding the balanced modes, we do not only look for structures which are controllable (by the actuator) but also observable by the sensor. Consequently, the balanced modes not only include information from the input but also from the output. As we will see in the rest of this section, it is possible to identify the flow structures to which the sensor is most sensitive through the adjoint Navier-Stokes equations. This is performed analogously in the frequency domain by computing the harmonic flow states which yield the maximum energy contribution to the sensor energy. Such harmonic flow structures, once computed on a frequency interval, are included in the balanced truncation procedure in order to find equally controllable and observable modes on the considered frequency interval.

In the end, the POD modes only include information from the actuator and the flow dynamics; they depend on the operators A and B . On the other hand, the balanced modes also rely on the sensor and depend on all three operators A , B , and C . By construction, the balanced modes are expected to be superior to the POD modes in capturing the input-output behavior since they include additional information from the original input-output system. Concerning linear unstable systems, the concepts of controllability and observability are no longer defined, neither are the harmonic responses of the system to harmonic forcings. However, the overall procedure introduced above will be shown to remain tractable, as illustrated later in Sec. IV.

How to obtain the POD and balanced modes stands for our next concern. In the following, the balanced modes, which rely on both the concepts of controllability and observability, are first introduced. The presentation of the POD modes (most controllable modes) is then given in a second step.

B. Balanced model reduction

1. Controllability and observability Gramians

Balanced truncation originally emerged from the control theory literature²⁹ as a way to reduce linear input-output systems such as Eq. (5) while quasi-optimally preserving its input-output behavior. Indeed, a useful property of balanced truncation is that it yields a priori error bounds on the transfer function that are close to the lower bound achievable by any reduced-order model. It is conceptually expressed in terms of controllability and observability of the modes used in the model reduction process. A specific state is deemed controllable if there exists a control law $c(t)$ which is able to modify the flow from any state toward this specific state. For controllable states, the notion of controllability then quantifies how easy (or difficult) the state can be reached from any state. Similarly, observability measures how easy (or difficult) a given flow state can be detected by the sensors. At the sensor location, almost unobservable flow states leave hardly any footprint behind and are thus nearly invisible to the measurement efforts. The key idea of balanced truncation is to compute rank and select modes that are equally observable and controllable in order to project the full original system

onto them. For a given flow state, the mathematical quantities that enable measuring these two properties are the controllability and observability Gramians G_c and G_o . Considering our input-output system (5) with a stable dynamical operator A , these Gramians are defined by

$$\begin{cases} G_c = \int_0^{+\infty} e^{At} B B^* e^{A^* t} dt \\ G_o = \int_0^{+\infty} e^{A^* t} C^* C e^{At} dt \end{cases} \quad (8)$$

For unstable systems, this definition does not hold since the integrals are not convergent anymore as $t \rightarrow \infty$. Yet, one may use a frequency domain definition of the Gramians, as proposed by Zhou *et al.*,³⁹ in order to avoid this problem

$$\begin{cases} G_c = \frac{1}{2\pi} \int_{-\infty}^{+\infty} (j\omega I - A)^{-1} B B^* (-j\omega I - A^*)^{-1} d\omega \\ G_o = \frac{1}{2\pi} \int_{-\infty}^{+\infty} (-j\omega I - A^*)^{-1} C^* C (j\omega I - A)^{-1} d\omega \end{cases} \quad (9)$$

It can be shown by using Parseval's theorem that the two definitions are equivalent for stable systems.^{39,41} It has been furthermore demonstrated³⁹ that the frequency domain definition (9) still works for unstable systems as far as there are no marginal modes and that balanced truncation is then equivalent to separating the stable and unstable parts of the transfer function and doing the balanced realization for both parts separately.

A technique referred to as balancing consists in finding flow fields with equal emphasis on either controllability or observability property. This latter is mathematically equivalent to finding a transformation basis in which the Gramians G_c and G_o appear diagonal and equal.⁶ Otherwise, these balanced modes can also be directly computed as the eigenvectors of the product of the two previously defined Gramians.²⁹ However, this is not computationally tractable for the complex flows considered here where the number of degrees of freedom is of order $O(10^{5-6})$. For systems of large dimension such as those encountered here, the Gramians are huge matrices which cannot be easily computed or stored. Instead, the algorithm introduced by Rowley³⁵ and referred to as BPOD approximates balanced truncation while remaining tractable even for very large systems and relies on the use of flow state snapshots.

2. Introduction of the frequential snapshots

To compute the balanced modes by a low-cost algorithm, a technique introduced by Rowley³⁵ consists in factoring the controllability and observability Gramians using flow state snapshots. Until now, the snapshot technique was achieved by considering the temporal expressions (8) of the Gramians, as in the original method of Rowley³⁵ or more

recent works.^{13-15,37} This approach is not adopted in our work. In this paper, the frequential expressions of the Gramians (8) are considered instead. Thus, introducing the flow states $\hat{X}_1(\omega)$ and $\hat{Y}_1(\omega)$ defined by

$$\hat{X}_1(\omega) = (j\omega I - A)^{-1} B, \quad (10a)$$

$$Q_1 \hat{Y}_1(\omega) = (-j\omega I - A^*)^{-1} C^*, \quad (10b)$$

the frequential expressions of the Gramians (9) reduce to

$$G_c = \frac{1}{2\pi} \int_{-\infty}^{+\infty} \hat{X}_1 \hat{X}_1^*(\omega) d\omega \approx \frac{1}{2\pi} \sum_{i \in \mathbb{Z}} \hat{X}_1 \hat{X}_1^*(\omega_i) \delta_i, \quad (11a)$$

$$\begin{aligned} G_o &= Q_1 \left(\frac{1}{2\pi} \int_{-\infty}^{+\infty} \hat{Y}_1 \hat{Y}_1^*(\omega) d\omega \right) Q_1 \\ &\approx Q_1 \left(\frac{1}{2\pi} \sum_{i \in \mathbb{Z}} \hat{Y}_1 \hat{Y}_1^*(\omega_i) \delta_i \right) Q_1, \end{aligned} \quad (11b)$$

where $\{\omega_i, i \in \mathbb{Z}\}$ is a given set of discrete pulsations and δ_i denotes appropriate quadrature coefficient. Note that \hat{X}_1 and \hat{Y}_1 are complex vector fields such that

$$\overline{\hat{X}_1(\omega_i)} = \hat{X}_1(-\omega_i), \quad (12a)$$

$$\overline{\hat{Y}_1(\omega_i)} = \hat{Y}_1(-\omega_i), \quad (12b)$$

where $\bar{\cdot}$ denotes the complex conjugate so that we can further expand Eqs. (11) to

$$G_c \approx \frac{1}{\pi} \sum_{i \in \mathbb{N}} [\hat{X}_{1r} \hat{X}_{1r}^*(\omega_i) + \hat{X}_{1i} \hat{X}_{1i}^*(\omega_i)] \delta_i, \quad (13a)$$

$$G_o \approx Q_1 \left(\frac{1}{\pi} \sum_{i \in \mathbb{N}} [\hat{Y}_{1r} \hat{Y}_{1r}^*(\omega_i) + \hat{Y}_{1i} \hat{Y}_{1i}^*(\omega_i)] \delta_i \right) Q_1, \quad (13b)$$

where we have introduced their real parts \hat{X}_{1r} , \hat{Y}_{1r} and their imaginary parts \hat{X}_{1i} , \hat{Y}_{1i} . In practice, the set of frequencies $\{\omega_i\}$ is finite so that only a finite interval of frequencies is considered. The numbers of real direct (\hat{X}_{1r} , \hat{X}_{1i}) and adjoint (\hat{Y}_{1r} , \hat{Y}_{1i}) flow states used in the process are denoted by n_d and n_a , respectively (both are even). As a result, the controllability and observability Gramians may be factored as

$$G_c \approx \mathbf{X}_1 \mathbf{X}_1^*, \quad (14a)$$

$$G_o \approx Q_1 \mathbf{Y}_1 \mathbf{Y}_1^* Q_1, \quad (14b)$$

by stacking these states as columns of the matrices \mathbf{X}_1 and \mathbf{Y}_1 as follows:

$$\mathbf{X}_1 = \frac{1}{\sqrt{\pi}} [\hat{X}_{1r}(\omega_0) \sqrt{\delta_0} \quad \hat{X}_{1i}(\omega_0) \sqrt{\delta_0} \quad \hat{X}_{1r}(\omega_1) \sqrt{\delta_1} \quad \hat{X}_{1i}(\omega_1) \sqrt{\delta_1} \dots], \quad (15a)$$

$$\mathbf{Y}_1 = \frac{1}{\sqrt{\pi}} [\hat{Y}_{1r}(\omega_0) \sqrt{\delta_0} \quad \hat{Y}_{1i}(\omega_0) \sqrt{\delta_0} \quad \hat{Y}_{1r}(\omega_1) \sqrt{\delta_1} \quad \hat{Y}_{1i}(\omega_1) \sqrt{\delta_1} \dots], \quad (15b)$$

where the dimension of \mathbf{X}_1 is $n_1 \times n_d$ and that of \mathbf{Y}_1 is $n_1 \times n_a$. Interestingly, the flow state $\hat{\mathbf{X}}_1(\omega)$ is solution (see Appendix B1) of the following direct problem:

$$\left[j\omega \begin{pmatrix} Q_1 & 0 \\ 0 & 0 \end{pmatrix} - \begin{pmatrix} A_1 & A_2^* \\ A_2 & 0 \end{pmatrix} \right] \begin{pmatrix} \hat{\mathbf{X}}_1 \\ \hat{\mathbf{X}}_2 \end{pmatrix} = \begin{pmatrix} Q_1 & 0 \\ 0 & 0 \end{pmatrix} \begin{pmatrix} B_1 \\ 0 \end{pmatrix} \quad (16a)$$

emphasizing that this state reduces to the harmonic flow response resulting from the forcing of the linear Navier-Stokes equations with an harmonic momentum actuation $(B_1, 0)$ of pulsation ω . Analogously, it is shown in Appendix B2 that $\hat{\mathbf{Y}}_1(\omega)$ is the solution of the following adjoint problem:

$$\begin{aligned} & \left[-j\omega \begin{pmatrix} Q_1 & 0 \\ 0 & 0 \end{pmatrix} - \begin{pmatrix} A_1^* & A_2^* \\ A_2 & 0 \end{pmatrix} \right] \begin{pmatrix} \hat{\mathbf{Y}}_1 \\ \hat{\mathbf{Y}}_2 \end{pmatrix} \\ & = \begin{pmatrix} Q_1 & 0 \\ 0 & 0 \end{pmatrix} \begin{pmatrix} Q_1^{-1} C_1^* \\ 0 \end{pmatrix} \end{aligned} \quad (17a)$$

pointing out that this adjoint state stands for the harmonic response flow state resulting from the forcing of the adjoint linear Navier-Stokes equations with a harmonic momentum actuation $(Q_1^{-1} C_1^*, 0)$ of pulsation ω . Hereafter, these direct and adjoint flow states are referred to as frequential snapshots in order to draw a parallel with existing time-domain definitions of the Gramians and associated temporal snapshots.

3. Computation of the balanced basis

The approximate Gramians (14) are not actually computed due to the large storage cost, but the leading modes of the transformation that balances these Gramians are computed using a cost-efficient algorithm introduced by Laub *et al.*³² and detailed below. It involves computing the singular value decomposition of the direct \mathbf{X}_1 and adjoint \mathbf{Y}_1 snapshots cross product $\mathbf{Y}_1^* Q_1 \mathbf{X}_1$, which is of size $n_a \times n_d$,

$$\mathbf{Y}_1^* Q_1 \mathbf{X}_1 = \mathbf{M} \mathbf{\Sigma} \mathbf{N}^* \quad (18)$$

where \mathbf{M} and \mathbf{N} are orthogonal matrices ($\mathbf{M}^* \mathbf{M} = \mathbf{I}$, $\mathbf{N}^* \mathbf{N} = \mathbf{I}$) of dimension $n_a \times n_a$ and $n_d \times n_d$, while $\mathbf{\Sigma}$ is diagonal and of size $n_a \times n_d$. For the fluid systems we are interested in, the typical number of snapshots is of order $O(10^{2-4})$, thus resulting in a reasonable computational cost. In a final step, denoting the balanced basis by the matrix \mathbf{T}_1 and its bi-orthogonal set by \mathbf{S}_1 , we have

$$\mathbf{T}_1 = \mathbf{X}_1 \mathbf{N} \mathbf{\Sigma}^{-1/2}, \quad (19a)$$

$$\mathbf{S}_1 = \mathbf{Y}_1 \mathbf{M} \mathbf{\Sigma}^{-1/2}. \quad (19b)$$

It is easily confirmed that the bi-orthogonality condition $\mathbf{S}_1^* Q_1 \mathbf{T}_1 = \mathbf{I}$ is satisfied and that, once transformed into these bases, the Gramians G_c and G_o appear diagonal and equal to $\mathbf{\Sigma}$

$$(\mathbf{Q}_1 \mathbf{S}_1)^* G_c (\mathbf{Q}_1 \mathbf{S}_1) = \mathbf{\Sigma}, \quad (20a)$$

$$\mathbf{T}_1^* G_o \mathbf{T}_1 = \mathbf{\Sigma}, \quad (20b)$$

and also that they are the eigenvectors of their product,

$$G_c G_o \mathbf{T}_1 = \mathbf{T}_1 \mathbf{\Sigma}^2, \quad (21a)$$

$$G_o G_c (\mathbf{Q}_1 \mathbf{S}_1) = (\mathbf{Q}_1 \mathbf{S}_1) \mathbf{\Sigma}^2. \quad (21b)$$

The diagonal entries of the transformed Gramians $\mathbf{\Sigma}$, called Hankel singular values (HSVs), decrease monotonically and are directly related to the controllability and observability of the corresponding states. It can be shown³⁵ that the columns of \mathbf{T}_1 form the first columns of the balancing transformation and the columns of $\mathbf{Q}_1 \mathbf{S}_1$ constitute the first columns of the inverse transformation.

C. POD model reduction

For the sake of completeness, POD modes are also considered in this study and their ability to capture the input-output dynamics is evaluated and compared to that of BPOD models. For stable systems, we have previously introduced the POD modes as the most controllable modes relative to the actuator. This means that they stand for the structures, the most easily triggered by the actuation. The POD modes, denoted by the matrix \mathbf{R}_1 , are given by the eigenvectors of the product $G_c Q_1$ ^{15,35} that is,

$$G_c Q_1 \mathbf{R}_1 = \mathbf{R}_1 \mathbf{\Lambda} \quad (22)$$

where the diagonal entries of the matrix $\mathbf{\Lambda}$ are called the POD eigenvalues. The POD eigenvalues decrease monotonically and are directly related to the controllability of the corresponding modes. Their computation is performed by using the classical snapshot method introduced by Sirovich.¹⁷ We have previously shown that $G_c = \mathbf{X}_1 \mathbf{X}_1^*$, where the collected dataset \mathbf{X}_1 stands for the direct frequential snapshots. We proceed by computing the eigenvalue decomposition of the product $\mathbf{X}_1^* Q_1 \mathbf{X}_1$, which is of size $n_d \times n_d$, by $\mathbf{X}_1^* Q_1 \mathbf{X}_1 = \mathbf{L} \mathbf{\Lambda} \mathbf{L}^*$, where \mathbf{L} is orthogonal ($\mathbf{L}^* \mathbf{L} = \mathbf{I}$). The POD modes can then be computed by

$$\mathbf{R}_1 = \mathbf{X}_1 \mathbf{L} \mathbf{\Lambda}^{-1/2}. \quad (23)$$

Note that, as expected, the POD modes are orthogonal with respect to the kinetic energy inner product, that is, $\mathbf{R}_1^* Q_1 \mathbf{R}_1 = \mathbf{I}$. It should be emphasized at this stage that this definition of the POD modes is not general since the considered dataset \mathbf{X}_1 is directly linked to the input $(B_1, 0)$ location. Reduced-order models are obtained by a Galerkin projection of the initial full system onto the modes with the highest POD eigenvalues. The procedure is similar to that described in Sec. II A 2, where we substitute \mathbf{T}_1 and \mathbf{S}_1 by \mathbf{R}_1 in Eq. (7).

D. Discussion

1. Practical considerations

Frequency information may be the most accessible quantity from many mechanical systems. In fluid mechanics, a physical interpretation of the flow behavior often relies on the frequency decomposition of its response to different forcings. For instance, some flows may behave as ‘‘oscillators’’

which impose their own frequency on the intrinsic dynamics, insensitively to external noise. On the other hand, some flows known as “noise-amplifiers” selectively amplify upstream noise, which often leads to a broad-band low-frequency spectrum of the downstream flow response. Due to this natural way to describe unsteady flows, frequency-based methods play a central role in the design of low-order models. Let us mention some examples such as the dynamic mode decomposition (DMD),^{43,44} which decomposes dynamical modes in the frequency domain or also the partitioning of modes into low, dominant, and high frequency in view of designing robust ROMs.^{19,21,45}

Concerning our linear state space formulation, the excitation by the actuator over a frequency interval is a way of extracting relevant information about the flow dynamics. Similarly, the adjoint frequency snapshots are introduced as a way to extract sensitivity information of the sensor over the same range of frequency. From an experimental point of view, the direct snapshots may be naturally obtained from harmonic excitations from the actuator. Suppose that the actuation law is given by $B \cos(\omega t)$, then the associated harmonic response of the flow will be given by $\tilde{X}_{1r}(\omega) \cos(\omega t) - \tilde{X}_{1i}(\omega) \sin(\omega t)$. Accordingly, the direct snapshots \tilde{X}_{1r} and \tilde{X}_{1i} may be simply recovered by extracting the flow states at successive times t and $t + T/4$, where $T = 2\pi/\omega$ is the period of the flow. The procedure to approximate the balanced modes requires the knowledge of adjoint states which cannot be directly extracted from experiments. However, we refer interested readers to the recent attempts to determine balanced ROMs without having to resort to adjoint information reported by Or and Speyer⁴⁶ and Ma *et al.*⁴⁷

An important point should also be noticed at this stage: Secs. III and IV include comparisons between POD and BPOD models in terms of modeling the input-output dynamics. As already mentioned earlier, the balanced modes are superior to the POD modes to reach this goal since they are conceptually designed to do so. However, even if BPOD models may yield the correct input-output dynamics, there is no guarantee that the original flow state may be captured. On the contrary, POD modes are meant to gradually capture the energy of the flow response in order to accurately recover its associated flow field, or at least its predominant energetic patterns. In fact, the superiority of the BPOD models comes from their potential to represent non-physical flow states which yield the correct input-output signal.

2. Computation of the snapshots

As previously mentioned, the snapshot method was achieved by considering the temporal expressions of the Gramians. Technically, the impulse response required to compute these temporal snapshots are computed by a direct and adjoint direct numerical simulation of the linearized Navier-Stokes equations. This time-stepping approach has been used so far in previous works on BPOD model reduction to yield the terms $e^{At}B$ and $e^{A^*t}C^*$. On the contrary, in a frequential framework, the snapshots correspond to harmonic responses to harmonic forcings. In this case, one has to invert a direct

and adjoint system to get the terms $(j\omega I - A)^{-1}B$ and $(-j\omega I - A^*)^{-1}C^*$ for each selected frequency ω . The large-scale matrices associated with these systems, which are of size $n_1 \times n_1$ here, are often sparse (depending on the numerical method used). The availability of efficient methods to inverse these huge systems is thus of utmost importance if one plans to adopt this strategy. Practically, the numerical methods to achieve these inversions can be either direct^{48,49} or iterative.⁵⁰ A valuable asset for proceeding in the frequential framework is the possibility to compute separately each snapshot, contrary to the time-stepping approach where the previous snapshots are required to compute the next one. This latter observation makes the frequential approach intrinsically fitted to parallel computation of the snapshots.

3. Fall-off of the snapshots norm

The snapshot method yields an approximation of the temporal [Eq. (8)] and frequential [Eq. (9)] expressions of the Gramians by discretizing and truncating the unbounded integrals to a maximum time and a maximum frequency, respectively. It is thus of primary interest to know how quickly does the norm of the snapshots cross-product within these integrals decrease at long times and high frequencies. It can easily be shown that the temporal snapshots norm decreases exponentially as $O(e^{-at})$ for long time where a is the growth rate of the least damped mode, whereas the frequential snapshots have an algebraic fall-off norm as $O(1/\omega^n)$ for high pulsation ($n=2$ in the case of the Navier-Stokes equations due to viscous terms). This point leads to the first conclusion that, for any stable system ($a < 0$), the temporal snapshots norm fall-off in time always become faster, for sufficiently long time, than the frequential snapshots norm fall-off in frequency. In spite of this observation, it is not possible to say in general if one approach would require less snapshots than the other one. All the same, it should be emphasized that, in a majority of fluid mechanics problems, the frequential responses norm remains centered and peaked at a well specified frequency corresponding physically to the promoting of natural hydrodynamic instabilities. This robust observation can be supported by mentioning the cases of boundary layers, separated flows, or wake flows that are subject, respectively, to the Tollmien-Schlichting, the Kelvin-Helmholtz, and the Benard-von Kàrmàn instabilities. In this framework, the frequential approach may be very appreciative for weakly stable systems, i.e., for systems where a is close to 0. In these cases, the impulse response relaxation time is very high so that the temporal approach would require very long time stepping simulations to compute the snapshots while the frequential responses would remain peaked at a given low frequency.

E. Numerical methods

Our numerical approach is based on a finite element method. All the equations are first rewritten in a variational formulation and then spatially discretized using a mesh composed of triangular elements. In particular, the velocity fields are projected onto six-node quadratic triangular elements with quadratic interpolation (P2-elements), whereas the

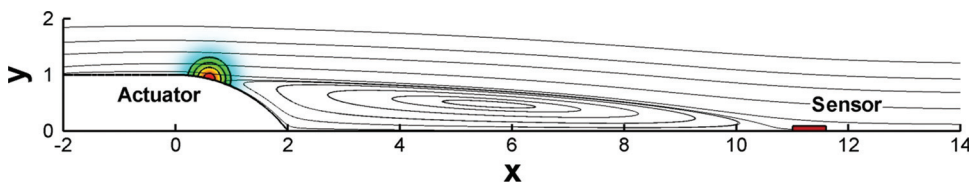


FIG. 1. (Color online) Streamlines of the base flow at $Re = 600$. The actuator and sensor locations are also depicted.

pressure field is discretized using three-node linear triangular elements (P1-elements). All the discrete matrices resulting from the projection of the variational formulations onto the basis of finite elements are sparse; they are built with the FreeFem++ software (<http://www.freefem.org>).

The frequential snapshots $\hat{X}_1(\omega_i)$ and $\hat{Y}_1(\omega_i)$ at discrete pulsations ω_i are obtained by inverting the linear systems (16) and (17). These snapshots are then recombined to compute the matrices \mathbf{X}_1 and \mathbf{Y}_1 by using an equidistant spacing $\Delta\omega$ between the snapshots and quadrature coefficients δ_i corresponding to the fourth-order Simpson method. The matrix inversion required to compute these snapshots are handled through a direct multifrontal sparse LU solver (MUMPS (Ref. 49)). Hence, the cost of this algorithm is approximately given by the cost of the LU decomposition of a large sparse complex matrix since the following successive inverses are cheap.

III. GLOBALLY STABLE CASE: THE ROUNDED BACKWARD-FACING STEP FLOW

Here, we provide an example of BPOD/POD model reduction using the snapshot method in the frequency domain as described in Sec. II. The case of a globally stable flow is first studied in this section by considering the input-output dynamics over a backward-facing step flow.

A. Flow configuration

We consider the two-dimensional rounded backward-facing step depicted in Figure 1. It consists of a circular part designed so that its length is twice its height (this geometry stems from the experimental work of Duriez⁵¹). The upstream velocity and the step height are used to make all quantities non-dimensional. The beginning and ending of the step are located at $(x=0, y=1)$ and $(x=2, y=0)$. The upstream, downstream, and upper boundaries are, respectively, located at $x=-20$, $x=100$, and $y=20$. A uniform and unitary velocity field ($u=1, v=0$) is prescribed at the inlet boundary ($x=-20$) and a laminar boundary layer starts developing on the lower boundary at $(x=-2, y=1)$. A free-slip condition with zero tangential stress ($\partial_y u = 0, v = 0$) is prescribed on the boundary ($-20 \leq x \leq -2, y = 1$). No-slip boundary conditions ($u=0$) are imposed on $(-2 \leq x \leq 0, y=1)$, on the step wall, and on the downstream wall ($2 \leq x \leq 100, y=0$). Symmetry boundary conditions are used at the upper boundary and a free outflow condition $p\mathbf{n} - Re^{-1}(\nabla\mathbf{u}) \cdot \mathbf{n} = 0$ is used at the outlet (\mathbf{n} being the outward normal unitary vector of the boundary).

The resulting base flow is computed by solving a Newton-Raphson method.⁵² We choose a Reynolds number $Re = 600$ where the flow is globally stable to two-dimensional

perturbations, and its corresponding base flow is represented in Figure 1. The displacement thickness at $x=0$ is $\delta^* \approx 0.082$, leading to a Reynolds number based on the displacement thickness of $Re_{\delta^*} \approx 49.2$. This choice of parameters rules out instabilities related to the boundary layer dynamics. The boundary layer separates at $x \approx 0.6$ and reattaches at $x \approx 11$ exhibiting a long shear layer responsible for strong transient growths. The input-output behavior is investigated by introducing one actuator and one sensor as sketched in Figure 1. The actuator is located on the step, just before the boundary layer separation, so as to trigger the most efficient response and the sensor is placed downstream, in the vicinity of the reattachment point. Once discretized, the equations governing the dynamics of small perturbations with actuation and sensing are given by the linear input-output system previously introduced in Eqs. (5). The actuator B stands for a volume forcing of Gaussian shape on the vertical velocity component centered on the step wall at $x=0.6$, with a width of 0.6 and a height of 1. As the measured quantity, we consider the wall-normal shear stress evaluated at and integrated over a localized region of the wall (the sensor location) so that $m(t) = \int_{x=11}^{x=11.6} \partial_y u dx$, which yields the vector C .

To give an idea, a typical discretization yields $n_1 \approx 360\,000$ degrees of freedom stemming from about 90 000 triangles.

B. Frequential snapshots

The frequential direct and adjoint snapshots required for the model reduction are computed by solving Eqs. (16) and (17). We have computed 399 equispaced complex frequential snapshots \hat{X}_1 and \hat{Y}_1 from $\omega = 0$ to $\omega = 4$ (resulting in $n_d = n_a = 798$).

As expressed in Sec. II, the direct snapshots correspond to the long time responses of the system to harmonic forcings of pulsation ω from the input location. We have represented in Figure 2(a), the evolution of the kinetic energy of the direct snapshots $\|\hat{X}_1\|^2 = \hat{X}_1^* Q_1 \hat{X}_1$ as a function of ω to highlight the noise amplifier behavior of this flow. The most amplified frequency $\omega \approx 0.72$ is associated with the Kelvin-Helmholtz instability of the separated shear layer. Figures 2(b)–2(e) depict the real part of the longitudinal velocity of the direct snapshots \hat{X}_1 for different frequencies. As expected, the corresponding patterns extend downstream from the actuator through the shear layer. The triggered wavepackets shown on these figures exhibit a spatial support that strongly depends on ω . Excitation to higher frequencies leads to smaller flow structures and to a faster diffusion. In particular, the highest frequency responses remain spatially localized in the vicinity of the actuator while the smallest frequency responses are widely extended downstream.

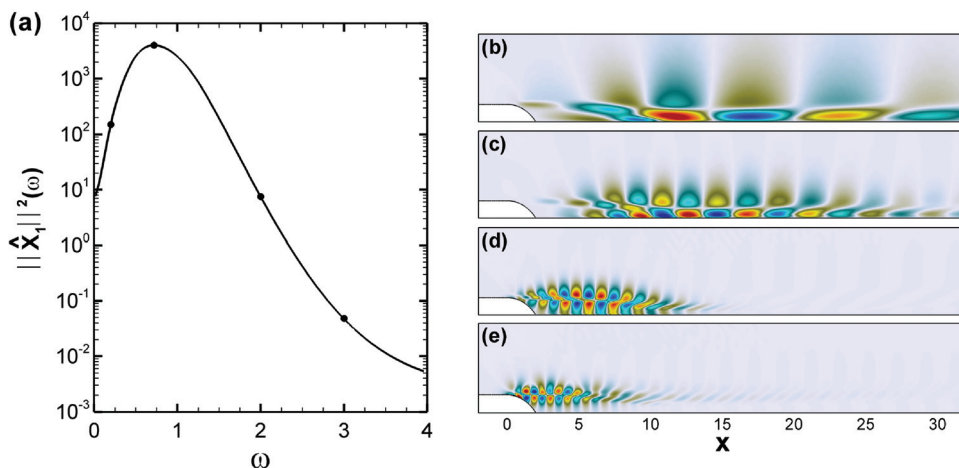


FIG. 2. (Color online) The left plot (a) shows the energy of the direct snapshots \hat{X}_1 as a function of ω . (b), (c), (d), (e) represent the real parts of the longitudinal velocity of the direct snapshots associated with the frequencies $\omega_i = 0.2, 0.72, 2,$ and 3 , respectively.

Figure 3 is devoted to the same purpose for the adjoint snapshots. In a similar manner, the adjoint snapshots correspond to the long time responses of the adjoint system to a harmonic forcing of pulsation ω from the sensor. The energy $\|Q_1 \hat{Y}_1\|^2$ displays a peak at a nearby frequency of $\omega \approx 0.64$, and analogously, the adjoint flow patterns are convected backward in time from the sensor to the upstream flow. A physical interpretation of the adjoint snapshots may arise by considering the transfer function of the system (5). The transfer function $\hat{G}(\omega)$ links the Fourier transform of the input $\hat{u}(\omega)$ to that of the output $\hat{m}(\omega)$ by

$$\hat{m}(\omega) = \hat{G}(\omega)\hat{u}(\omega) \tag{24}$$

and can be computed by $\hat{G}(\omega) = C(j\omega I - A)^{-1}B$ or, introducing the adjoint snapshot $\hat{Y}_1(\omega)$, by

$$\hat{G}(\omega) = \hat{Y}_1^*(\omega)Q_1B. \tag{25}$$

This means that, given a frequency ω_0 , the component $\hat{m}(\omega_0)$ of the measure is proportional to $\hat{Y}_1^*(\omega_0)Q_1B$, i.e., the inner product between the actuator B and the frequential snapshot $\hat{Y}_1(\omega_0)$. In other words, the flow structures excited by the output and shown in Figures 3(b)–3(e) are

also the states to which the sensor is the most sensitive at this given frequency excitation. In our case, we observe that these forcing structures leading to maximum measurements at the sensor are upstream-tilted patterns located along the shear layer. They are leant against the shear so as to optimally trigger the Orr mechanism and are then amplified through the shear layer. Analogously to the direct snapshots, the spatial support of the adjoint states strongly depends on ω . For higher frequencies, smaller flow structures are localized in the vicinity of the sensor due to a higher diffusion while smallest frequency responses are largely extended upstream.

C. Reduced-order models

The previously computed frequential snapshots are used within the procedure outlined in Sec. II to build BPOD/POD based reduced-order models. We have represented in Figure 4(a), the first 14 HSVs σ_j . As expressed in Sec. II, the HSVs provide a way to assess the controllability and observability of its associated modes. This quantity is naturally used to decide on a truncation point and thus on the size of the reduced-order models. A significant drop in the HSVs is observed and justifies the truncation of the balancing basis. Similarly, we have represented in Figure 4(d) the first 140 POD eigenvalues λ_j . Note that they rank the associated POD

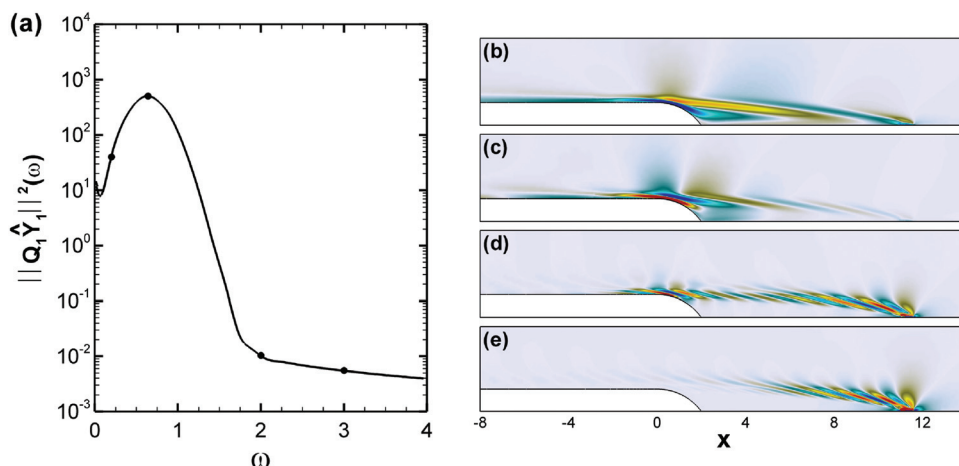


FIG. 3. (Color online) The left plot (a) shows the energy of the adjoint snapshots as a function of ω . Note that, owing to the definition (10) of the snapshots, the relevant quantity to be measured is $Q_1 \hat{Y}_1$. Figures (b), (c), (d), and (e) represent the real parts of the longitudinal velocity of the adjoint snapshots associated with the frequencies $\omega = 0.2, 0.64, 2,$ and 3 , respectively.

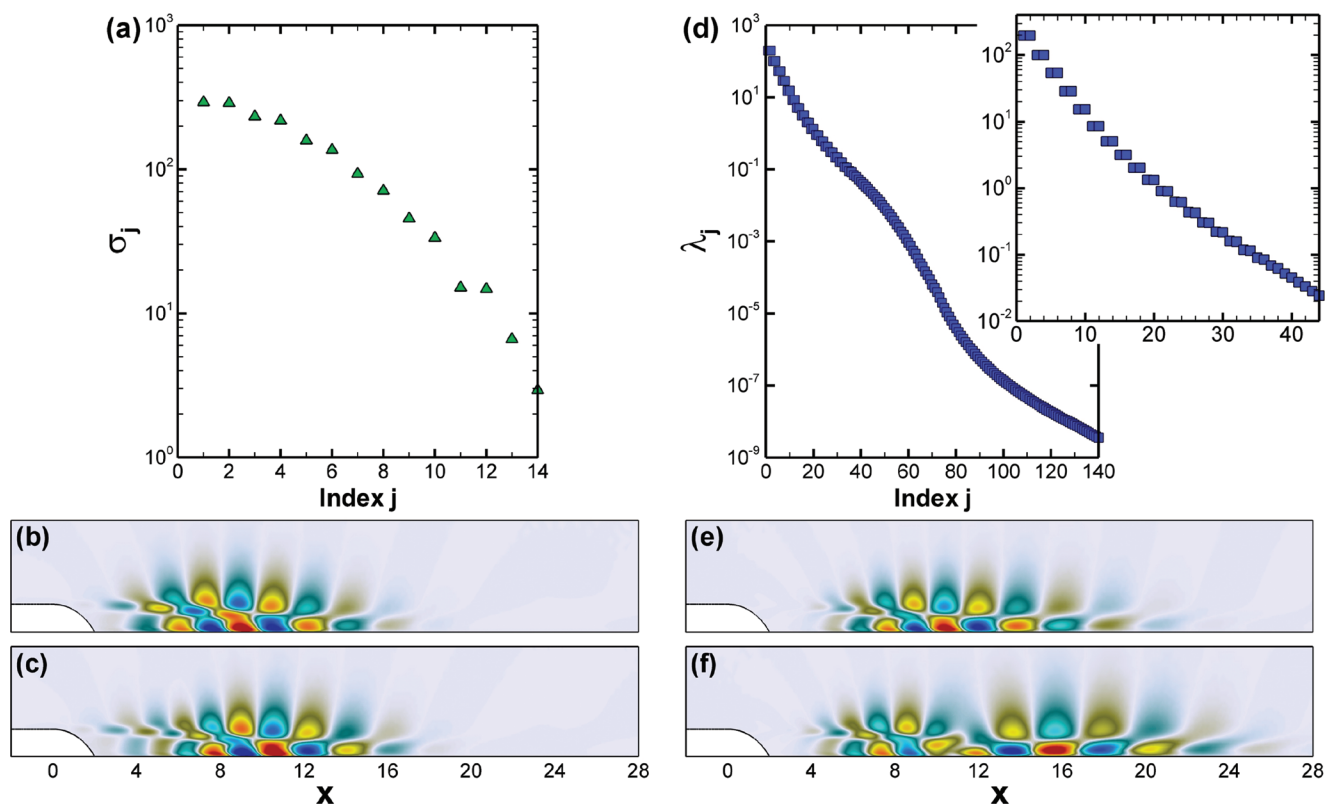


FIG. 4. (Color online) (a) First 14 HSVs σ_j and (d) first 140 POD eigenvalues λ_j . (b) and (c) stand for the streamwise velocity component of the first and third BPOD modes. Analogously, (e) and (f) stand for the first and third POD modes.

modes according to how easily they can be influenced by the input, i.e., their controllability. We have represented in Figures 4(b) and 4(c) the first and third BPOD modes, visualized by their streamwise velocity component. They consist of wavepackets resulting from the amplification of vortices along the shear layer and spatially localized between the actuator and the sensor. Figures 4(e) and 4(f) are devoted to the same purpose for the first and third POD modes. It should be noted that they reduce to the structures that are most easily influenced by the input. In other words, low energy is needed to force these large-scale structures downstream owing to the amplification provided by the intrinsic flow dynamics. They also appear as wavepackets but are somewhat more spatially extended downstream where the energy of the response to forcing is the largest. This latter observation is consistent with other recent works.^{13,38}

Interestingly, we notice a pairwise occurrence of the eigenvalues. Looking at Figure 4(a), the first 6 HSVs come in pairs while it is even more obvious in Figure 4(d) for the first 30 POD eigenvalues. According to the previous work of Aubry *et al.*⁵³ based on the time-space bi-orthogonal decomposition of complex signals,²⁰ the POD modes of a traveling wave consist of degenerated pairs of modes, having the same eigenvalues and having shifted spatial structures of one another. In our case, it is indeed recovered that the eigenmodes of a given pair are a quarter period out of phase. This result holds for both BPOD and POD modes. This confirms that our models are predominantly governed by the dynamics of traveling waves. Recalling that POD models are meant to recover the exact flow

field response, contrary to BPOD models (see Sec. II D 1), it is natural to observe a clearer representation of the original traveling wave packet in the case of POD modes. For higher BPOD or POD modes, the pairwise occurrence of the eigenvalues gradually vanishes. One may attribute this result to a deviation from traveling waves due to the modulation of the wave packet in the streamwise direction according to the work of Aubry *et al.*^{54,55}

It should be mentioned at this stage that our 399 complex and equally spaced snapshots are sufficient for accurate computation of the BPOD and POD modes, since for a larger number of snapshots, with finer spacing or larger frequency interval, there is no considerable change in the eigenvalue spectrum.

D. Impulse response and transfer function

By definition, the input-output behavior links the effect of the actuator on the flow to the information extracted by the sensor. It can be described by the impulse response or, equivalently, by the transfer function. The impulse response of a linear system is important, since the response of the system to any input can be found from the convolution of the impulse response with the input. The impulse response $G(t)$ of the full system is obtained numerically from a time-stepper simulation of the linearized Navier-Stokes equations (4) for the control law $c(t) = \delta(t)$, $\delta(t)$ being the Dirac function. In other words, the impulse response is $G(t) = CX_1(t)$, where $X_1(t)$ is solution of the initial-value problem

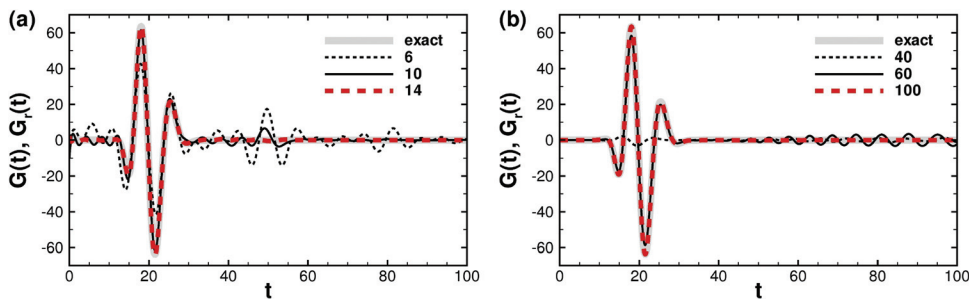


FIG. 5. (Color online) (a) Impulse response of the full system $G(t)$ and of the reduced-order models $G_r(t)$ for (a) BPOD models and (b) POD models.

$$\frac{dX_1}{dt} = AX_1, \tag{26a}$$

$$X_1(t=0) = B. \tag{26b}$$

The corresponding simulation is integrated in time using a second-order accurate scheme. The impulse responses of the ROMs $G_r(t)$ are computed directly by $G_r(t) = C_r e^{A_r t} B_r$, where A_r , B_r and C_r stand for the matrices A , B , and C projected onto r modes. Figures 5(a) and 5(b) display the impulse response of the full system and those of the BPOD and POD reduced-order models, respectively. The impulse response of BPOD models with $r=6$, $r=10$, and $r=14$ are represented in Figure 5(a) and those of POD models with $r=40$, $r=60$, and $r=100$ are represented in Figure 5(b). With $r=14$ BPOD modes or $r=100$ POD modes, we observe that reduced models register the same signal as the full model. The impulse at the actuator B generates a wavepacket that travels along the shear layer until it reaches the sensor at $t \approx 10$. The effect of this wavepacket is measured by the sensor until $t \approx 35$ and is then further convected downstream to eventually leave the computational domain.

Since all frequencies are equally excited by an initial impulse, a convenient and alternative way of expressing the input-output behavior of a linear system is to switch to the frequency domain. The frequency response of the full system and the ROMs are compared next. The transfer function of the full system is simply given by $\hat{G}(\omega) = \int_0^\infty e^{-j\omega t} G(t) dt$ while those of the ROMs are obtained, using equivalent notations, by $\hat{G}_r(\omega) = C_r (j\omega I_r - A_r)^{-1} B_r$, where I_r stands for the identity matrix of size r . Note that the exact transfer function is easily computed by measuring (multiplying by C) each already computed direct snapshots $\hat{X}_1^*(\omega_i) = (j\omega_i I - A)^{-1} B$. Figures 6(a) and 6(b) depict the absolute values of the transfer functions of the full system together with those of BPOD and POD models, respectively. We recover a preferred frequency around $\omega = 0.78$ which corresponds to the

pseudo-pulsation observed in Figure 5. Note that this pulsation is also associated with the amplification of the impulse perturbation through the shear layer due to the Kelvin-Helmholtz instability. In terms of models efficiency, the same conclusion arises since 14 BPOD and 100 POD modes are, respectively, sufficient to capture the most important trends of the input-output behavior.

For the sake of completeness, we also quantify the performance of the models in capturing the input-output behavior by computing the H_∞ relative norm of the error. For a model of size r , this error, denoted by $e_\infty(r)$, is given by

$$e_\infty(r) = \frac{\max_{\omega \in \mathbb{R}} |\hat{G}(\omega) - \hat{G}_r(\omega)|}{\max_{\omega \in \mathbb{R}} |\hat{G}(\omega)|}. \tag{27}$$

The choice of this norm is motivated by the availability of theoretical bounds on the discrepancy between the approximate and exact transfer functions for balanced truncation. In Figures 7(a) and 7(b), we have represented the error $e_\infty(r)$ for the BPOD and POD models, respectively. As expected, the error falls off in both cases, assessing the efficiency of these models. In particular, we observe that the number of required POD modes to reach a given error e_∞ is significantly higher than the number of required BPOD modes. Indeed, the BPOD error falls quite rapidly and remains bounded between the lower (valid for any ROM) and the upper (valid for balanced truncation models) theoretical bounds,^{35,41} given by

$$\sigma_{r+1} < \|\hat{G}(\omega) - \hat{G}_r(\omega)\|_\infty \leq 2 \sum_{j=r+1}^{n_1} \sigma_j \tag{28}$$

where n_1 is the dimension of the full system. We conclude that both models succeed in capturing the full input-output behavior of the system with a superiority of BPOD models over POD ones. This latter point is consistent with existing literature.¹⁵

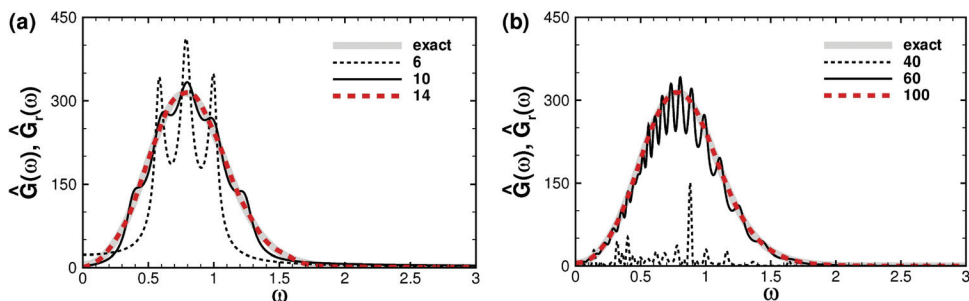


FIG. 6. (Color online) Transfer function of the full system $\hat{G}(\omega)$ and of the reduced-order models $\hat{G}_r(\omega)$ for (a) BPOD models and (b) POD models.

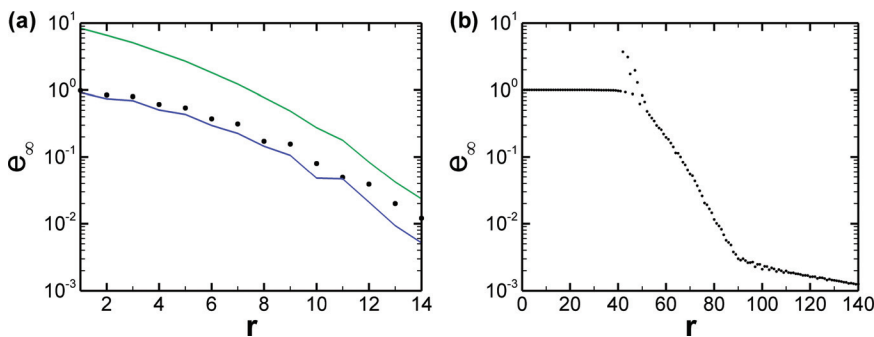


FIG. 7. (Color online) H_∞ Relative norm of the error e_∞ as a function of the size r of the reduced-order models for (a) the BPOD and (b) the POD modes. Note that the upper and lower bounds on the error, computed by Eq. (28), have been reported in (a) by solid lines.

IV. GLOBALLY UNSTABLE CASE: THE SQUARE CAVITY FLOW

Here, we deal with the case of a two-dimensional square cavity flow. We consider the same configuration, input and output as those used by Barbagallo *et al.*¹⁵ whose base flow exhibit eight unstable global modes. Due to the unstable nature of the flow, any initial disturbance is amplified, leading to large-amplitude perturbations for sufficiently large times. Recalling the linear dynamics assumption introduced in Sec. II, we are concerned here with the early development of the perturbations, i.e., the stage where the perturbation amplitude remains weak. In the reference work,¹⁵ the authors have designed reduced-order models for flow control purpose. Particularly, they showed that BPOD and POD modes were successful in capturing the input-output behavior of their flow. They used a snapshot method based on a temporal definition of the Gramians, restricting their approach to the stable subspace dynamics. Consequently, they had to model the unstable dynamics separately, using the unstable global modes. The second numerical example presented here is used as a reference case to show that frequential snapshots enable to reduce the system without separating the unstable and stable subspaces and that the resulting ROMs yield the correct full input-output dynamics (meaning both the correct stable and unstable input-output behaviors). To this end, we reduce the system using BPOD and POD modes, as in Sec. III, and we next compare our results to those of Barbagallo *et al.*¹⁵

A. Flow configuration

We briefly describe the flow configuration studied in this section. The square cavity flow of interest has first been introduced in Sipp and Lebedev⁵² where a more detailed description of the geometry and boundary conditions is available. It consists of a uniform incoming flow over a square cavity. The Reynolds number based on the uniform upstream velocity and cavity depth is fixed to $Re = 7500$. The corresponding base flow, defined as a solution of the steady Navier-Stokes equations, is displayed in Figure 8 by its streamlines together with the actuator and sensor location. Note that the boundary layer starts developing at $x = -0.4$ (the origin of the coordinate system coincides with the top left corner of the square cavity).

Regarding the input, Barbagallo *et al.*¹⁵ chose an actuator consisting of a parabolic normal velocity blowing near the upstream edge of the cavity, over the streamwise extent

($-7/20 \leq x \leq 0, y = 0$). Additionally, they adopted a transformation referred to as lifting in order to formulate the problem as a driven homogeneous state space system. We will not go into further details about this matter as it is not our point. Yet, it is important to note that their input B used to perform BPOD or POD ROMs is solution of the steady but inhomogeneous Navier-Stokes equations with boundary conditions given for ($-7/20 \leq x \leq 0, y = 0$) by the velocity profile

$$u(x, y = 0, t) = 0 \quad (29)$$

$$v(x, y = 0, t) = -\frac{x(1600x + 560)}{147}. \quad (30)$$

The solution of this steady problem and associated inhomogeneous boundary conditions constitutes the actuation which is referred to as the input B on the finite input-output system (5). The sensor is located near the downstream edge of the cavity, on the segment ($1 \leq x \leq 1.1, y = 0$). The output is the wall-normal shear stress evaluated at and integrated over a localized region of the wall

$$m(t) = \int_{x=1}^{x=1.1} \frac{\partial u}{\partial y} \Big|_{y=0}(t) dx. \quad (31)$$

Similarly, this measurement is expressed by the matrix C on the finite system (5), resulting from the discretization on a given mesh. Note that we choose the same numerical finite element approach based on the same non-structured triangular mesh as that used in Barbagallo *et al.*¹⁵ in order to avoid any numerical effect. This one results in $n_1 \approx 780\,000$ degrees of freedom stemming from about 200 000 triangles.

As previously mentioned, the base flow is globally unstable at $Re = 7500$. A global stability analysis of the flow

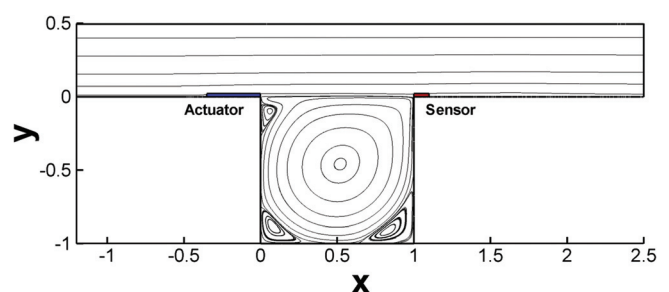


FIG. 8. (Color online) Streamlines of the base flow at $Re = 7500$. The actuator and sensor locations are also depicted.

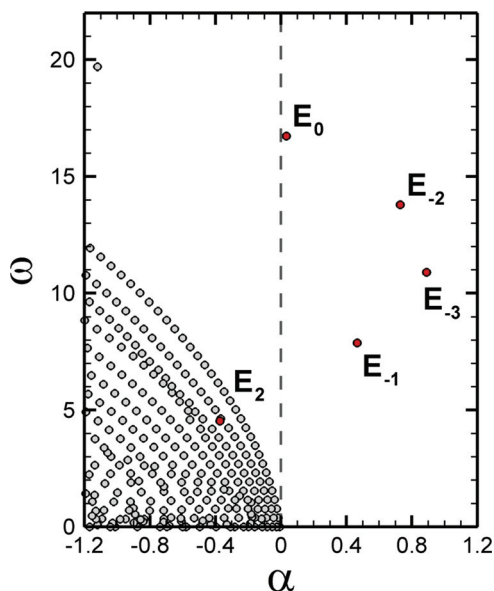


FIG. 9. (Color online) Part of the global eigenspectrum of the square cavity flow at $Re = 7500$ (taken from Barbagallo *et al.* (Ref. 15).

is presented in the work of Barbagallo *et al.*,¹⁵ and we briefly summarize their results here. The system of Eqs. (5) allows the computation of a temporal global spectrum and associated modes via the common assumption of an exponential time-dependence expressed as $\mathbf{X}_1(x, y, t) = \tilde{\mathbf{X}}_1(x, y)e^{i\gamma t}$, where $\gamma \in \mathbb{C}$ is the eigenvalue and $\tilde{\mathbf{X}}_1$ the eigenvector given by

$$A\tilde{\mathbf{X}}_1 = \gamma\tilde{\mathbf{X}}_1. \quad (32)$$

Eigenvalues are decomposed into $\gamma = \alpha + j\omega$, where α is the amplification rate and ω the pulsation so that unstable modes are characterized by $\alpha > 0$. The low-frequency part of the eigenspectrum, corresponding to the most unstable global modes, has been represented in Figure 9. This stability analysis displays four unstable “physical” global modes, i.e., eight if the complex conjugates are counted. These four unstable modes are denoted by E_{-3} , E_{-2} , E_{-1} , and E_0 as in the reference paper.¹⁵ Furthermore, we have also highlighted a stable global mode, denoted by E_2 , which displays¹⁵ a prominent contribution to the input-output dynamics. The role of this particular mode is illustrated below.

B. Frequential snapshots

Similarly to the flow over the backward-facing step, the frequential direct and adjoint snapshots required for the model reduction are computed by solving Eqs. (16) and (17). We have computed 499 equispaced complex frequential snapshots $\hat{\mathbf{X}}_1$ and $\hat{\mathbf{Y}}_1$ from $\omega = 0$ to $\omega = 35$, resulting in $n_d = n_a = 998$. Since the full system is unstable, these complex flow states can no longer be interpreted physically as long time responses to harmonic forcings. However, the inversion required to solve Eqs. (16) and (17) remain tractable as far as there are no marginal modes, which is the case here. We have represented in Figure 10 the evolution of the snapshots kinetic energy $\|\hat{\mathbf{X}}_1\|^2$ and $\|\mathbf{Q}_1\hat{\mathbf{Y}}_1\|^2$ as a function

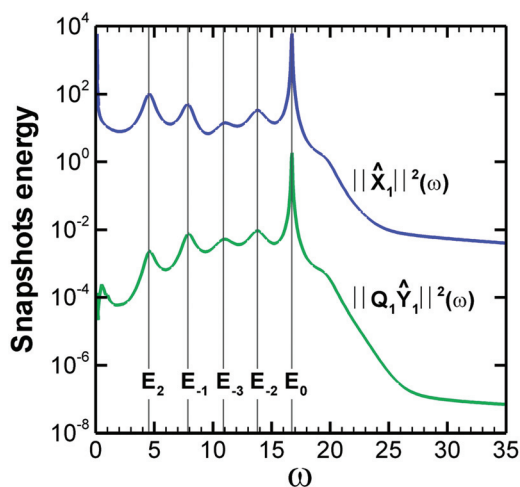


FIG. 10. (Color online) Energy of the direct $\hat{\mathbf{X}}_1$ and adjoint $\mathbf{Q}_1 \hat{\mathbf{Y}}_1$ snapshots as a function of ω . The lines indicate the frequencies of nearby global modes E_2 , E_{-1} , E_{-3} , E_{-2} , and E_0 (ordered from left to right).

of ω . We observe that both quantities display five peaks and eventually decrease quite abruptly for higher frequencies. These peaks are actually resulting from a pseudo-resonance with nearby global modes. This statement is argued by the representation of the frequencies of the corresponding global modes by dashed lines. To be more precise, the four highest frequencies depicted in Figure 10 correspond to the four isolated unstable global modes labeled E_{-3} , E_{-2} , E_{-1} , and E_0 in the reference work.¹⁵ Within this set, we observe that the modes having the smallest growth rate lead to the highest energy peak, emphasizing the pseudo-resonance phenomenon. As for the first low frequency peak at $\omega \approx 4.54$, it is related to the stable global mode E_2 . This particular mode has been shown¹⁵ to have an important contribution to the input-output behavior, more precisely, it is both strongly controllable and observable. Interestingly, we recover a peak of energy for both the direct and adjoint snapshots at its frequency.

C. Reduced-order models

Following the procedure introduced in Sec. II, the snapshots are used to build BPOD and POD based ROMs as in the case of the backward-facing step flow. The first 40 HSVs σ_j and first 200 POD eigenvalues λ_j computed for the square cavity flow are represented in Figures 11(a) and 11(b), respectively. Analogously to the results presented in Sec. III, a significant drop in the HSVs is observed and the first ones are seen to come in pairs due to the representation of traveling structures by the superposition of modes that are 90° out of phase. Moreover, the same observations hold for the POD eigenvalues. Similarly to the previous numerical example, it was found that the 499 computed snapshots are sufficient for an accurate computation of the BPOD/POD modes and eigenvalues.

The resulting ROMs defined by Eq. (6) are found to be unstable with both BPOD and POD models. In other words, the reduced matrices A_r now possess unstable eigenmodes, which is not surprising since the original system is unstable.

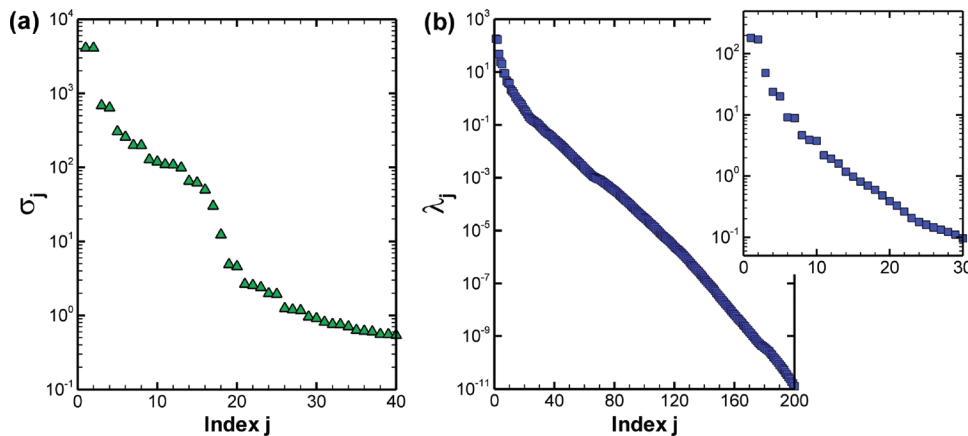


FIG. 11. (Color online) (a) First 40 HSVs σ_j and (b) first 200 POD eigenvalues λ_j .

For unstable systems, the usual transfer functions are no more defined. Yet, one can still compute the “frequency response” of the full unstable system $\hat{G}(\omega) = C(j\omega I - A)^{-1}B$ and of the ROMs $\hat{G}_r(\omega) = C_r(j\omega I_r - A_r)^{-1}B_r$ as long as there are no marginal modes. This latter quantity may be useful to assess the performance of the ROMs in capturing the full input-output dynamics, all the more so as Zhou *et al.*³⁹ demonstrated that the upper theoretical bound on the H_∞ transfer function error $e_\infty(r)$, given in Eq. (28), still holds for the balanced truncation of possibly unstable systems. We have represented in Figure 12 the relative error $e_\infty(r)$ defined by Eq. (27), in the case of the cavity flow together with theoretical bounds given by Eq. (28). The error is indeed observed to lie between these bounds and decrease while increasing the size r of the ROMs, linking favorably our results to theoretical predictions of Zhou *et al.*³⁹ This first result illustrates the relevancy and ability of BPOD models to capture the over-all input-output dynamics of our unstable system. However, we next provide a deeper insight into the performance of the BPOD and POD models to accurately model the unstable and stable input-output behavior. This issue has been largely investigated by Barbagallo *et al.*¹⁵ as they showed that the accurate modeling of each subspace is essential when it comes to effective closed-loop control design. As a result, particular attention is given to them in the remaining of this section.

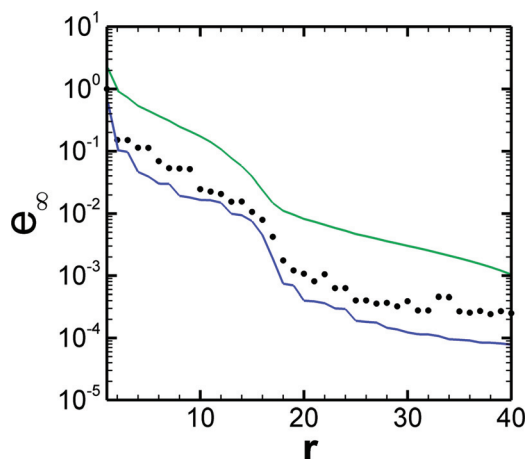


FIG. 12. (Color online) Relative error e_∞ as a function of the size r of the ROMs for the BPOD models. The upper and lower bounds on the error, computed by Eq. (28), are also displayed by the upper and lower solid lines.

1. Comparison of the unstable subspaces

Because of their ability to model the inherent instabilities and because of their low dimensionality, the unstable global modes come out as the most natural basis of the unstable subspace. Besides, Ahuja and Rowley¹⁴ and Barbagallo *et al.*¹⁵ directly used them to represent the dynamics of their unstable subspace, leading to an “exact” model since no modeling assumptions are invoked. The unstable dynamics of the ROMs is thus compared to the original one through their unstable modes.

The eigenspectrum and global modal decomposition of the ROMs is obtained by directly computing the eigenvalues/eigenvectors of the reduced matrix A_r . We have represented in Figure 13(a) the number of unstable eigenmodes as a function of the size r of the BPOD models. It is observed that models of sufficiently high size eventually exhibit eight unstable global modes just like the full system. The number of unstable modes rise quickly to reach eight for a model of size $r = 15$, which is highlighted on the figure by a dashed line. We note that BPOD models of size 24 and 32 possess nine unstable global modes which may be attributed to the sensitivity of the procedure to numerical issues.¹⁵ Figure 13(b) represents the same information for POD models. Similarly, the number of unstable modes rises until the value of eight but this increase is much more erratic than for BPOD models. Additionally, the model size required to get the eight unstable modes is $r = 82$ (depicted by a dashed line on the figure), which is far more important than for BPOD models.

The unstable part ($\alpha > 0$) of the eigenspectrum of the full system and those of several BPOD and POD models are depicted in Figures 14(a) and 14(b) respectively. Since all eigenspectrum are symmetric about the axis ($\omega = 0$), only the upper complex half-plan ($\omega > 0$) is represented. The computation of the full system eigenspectrum (and eigenvectors) is based on a classical shift and invert iterative Arnoldi algorithm and yields the same results as those in Barbagallo *et al.*¹⁵ The results on BPOD models, depicted in Figure 14(a), show that the unstable eigenvalues of the ROMs quickly tend to those obtained by Barbagallo *et al.*¹⁵ for the full system as the model size r is increased. As for POD models, a similar behavior is observed in Figure 14(b) though much more modes are required to recover the unstable global modes of the full system.

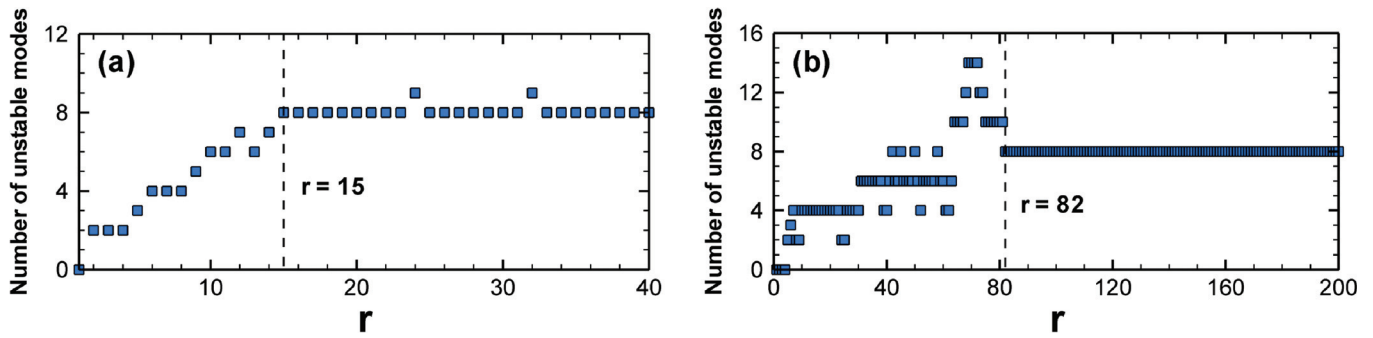


FIG. 13. (Color online) Number of unstable modes for (a) the BPOD models and (b) the POD models. Both ROMs exhibits eight unstable modes from the dashed lines standing for $r = 15$ and $r = 82$ respectively.

This convergence of the unstable eigenmodes is further outlined in Table I, where we have listed the growth rate α and pulsation ω of the unstable modes of the full system and those of several ROMs. Note that the column titled “Size” stands for the eigenvalue problem size, that is r for the ROMs and n_1 for the full system. We considered that the unstable modes labeled E_{-3} , E_{-2} , E_{-1} , and E_0 could be clearly identified for BPOD models with $r \geq 15$ and POD models with $r \geq 82$ as their unstable global modes frequency approximates correctly those of the full system with a two digits accuracy. The superiority of BPOD models over POD ones is more quantitatively illustrated by these results. Note that some further information on the eigenspectrum of POD models is provided in Appendix C.

We now turn our attention to the unstable subspaces. In our case, they are low dimensional (eight in the case of the full system), and their most natural basis is simply given by the unstable eigenvectors. By computing the unstable eigenvectors of the ROMs, we come to the conclusion that, for models of sufficient size, they match those of the full system once rebuilt in their original basis. This is illustrated in Figures 15(a) and 15(b), where we depict the real part of the longitudinal velocity of the most unstable global mode E_{-3} associated, respectively, with the full system and a POD model of size 150. Note that the mode built from the POD ROM is computed by $R_1 \tilde{X}_{1r}$ where \tilde{X}_{1r} is the reduced unstable eigenvector. The two resulting flow structures are observed to be almost indistinguishable. Furthermore, this latter observation holds (not shown here) for the three other unstable modes and for BPOD ROMs (computed by $T_1 \tilde{X}_{1r}$). In this subsection, we have thus

demonstrated that both the BPOD and POD procedures (for models of sufficient size) are successful in modeling the original unstable subspace insofar as the unstable subspace of the ROMs possesses the same natural basis.

2. Comparison of the stable input-output dynamics

The stable subspace is, as often, high dimensional and the main effort in reducing the system’s dimension is expended reducing the dynamics in the stable subspace. Furthermore, it contains substantial physical information about the input-output behavior we are interested in. Similarly to previous studies,^{14,15} we assess the accuracy of the ROMs in modeling the exact stable input-output dynamics by computing their stable transfer function.

The stable transfer function of the full system can be computed either by $\hat{G}_s(\omega) = C(j\omega I - A_s)^{-1}B$, where A_s is the restriction of A on its stable subspace, or by the Fourier transform of the stable impulse response defined by $G_s(t) = Ce^{A_s t}B$. In this work, the exact transfer function is taken from the work of Barbagallo *et al.*,¹⁵ where they adopted the second solution. As for the ROMs, the stable transfer functions $\hat{G}_{rs}(\omega)$ are directly computed by $\hat{G}_{rs}(\omega) = C_r(j\omega I_r - A_{rs})^{-1}B_r$, where A_{rs} is the restriction of A_r on its stable subspace. Figures 16(a) and 16(b) depict the transfer function of the full system superimposed on those of several BPOD and POD models respectively. It is observed to be very well approximated in both cases for ROMs of sufficiently high size. We recover a preferred frequency around $\omega = 4.6$, which corresponds to the

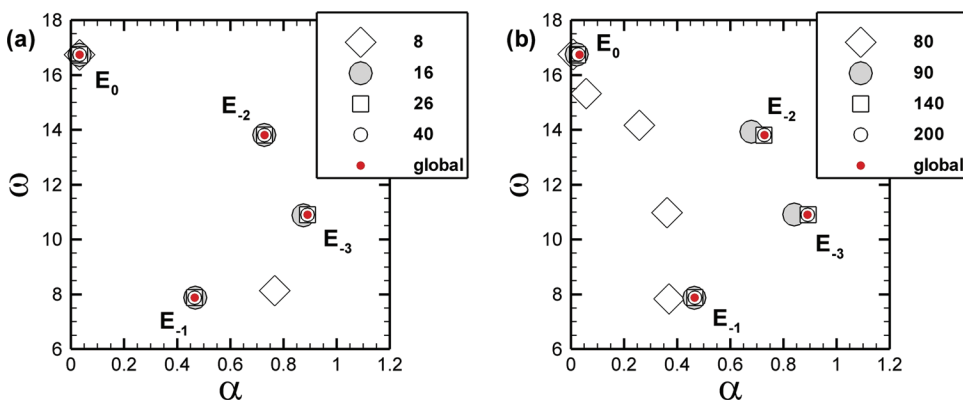


FIG. 14. (Color online) Unstable eigenspectrum of the full system versus those of (a) BPOD and (b) POD models.

TABLE I. Growth rate α and pulsation ω of the unstable modes labeled E_{-3} , E_{-2} , E_{-1} , and E_0 of the full system and those of several ROMs. The size column stands for the size r of the ROMs and is equal to n_1 for the full system.

	Size	E_{-3}		E_{-2}		E_{-1}		E_0	
		α	ω	α	ω	α	ω	α	ω
BPOD	15	0.874806	10.77852	0.723728	13.8188	0.464693	7.884405	0.032403	16.73146
	20	0.889216	10.8997	0.728018	13.8042	0.465734	7.88121	0.0324203	16.7315
	30	0.890282	10.9011	0.728619	13.8037	0.465488	7.88134	0.0324236	16.7315
	40	0.890204	10.9004	0.728317	13.8039	0.465577	7.88133	0.0324238	16.7315
POD	82	0.540170	10.93990	0.417714	14.20645	0.401845	7.842179	0.020019	16.74988
	120	0.915394	10.8931	0.748506	13.7754	0.47076	7.88286	0.0303051	16.7293
	160	0.88925	10.9022	0.722727	13.8058	0.466002	7.88255	0.0215329	16.7345
	200	0.891552	10.9028	0.727882	13.8094	0.466655	7.88173	0.0275948	16.7415
Full System	778 410	0.890451	10.9008	0.728513	13.8037	0.465557	7.88173	0.032426	16.7315

frequency of the stable mode E_2 and to the first peak observed in Figure 10. For a model of size r , this performance is quantified by computing the H_∞ relative norm of the error $e_{\infty s}(r)$ defined by

$$e_{\infty s}(r) = \frac{\max_{\omega \in \mathbb{R}} |\hat{G}_s(\omega) - \hat{G}_{rs}(\omega)|}{\max_{\omega \in \mathbb{R}} |\hat{G}_s(\omega)|}. \quad (33)$$

This error is plotted in Figures 17(a) and 17(b) for BPOD and POD ROMs, respectively. It is meant to convey the convergence behavior of the transfer functions of the ROMs as a function of the size r of the models. Similarly to the backward-facing step flow case, the error converges to zero as the number of modes increases and a faster error decrease is observed for BPOD models compared to POD ones.

Comparing these error convergence to those observed in Barbagallo *et al.*,¹⁵ we notice that both our BPOD/POD models require more modes to reach a given error $e_{\infty s}$. This is not surprising as our procedures perform the reduction of both the stable and unstable dynamics at the same time while theirs are focused on the stable dynamics. Given this fact, the performance of our models in capturing the correct stable input-output behavior is delayed compared to theirs due to the constraint of modeling the unstable subspace at the same time. This assertion is further argued in Figures 17(a) and 17(b), where we have drawn by dashed lines the limits $r=15$ and $r=82$ from which the models possess eight unstable global modes. We clearly notice a sudden fall-off on the error starting from these limits, that is, a sudden improvement of the models in capturing the stable input-output dynamics.

3. Assessment

We conclude from this section that both ROMs not only succeed in capturing the full unstable subspace but also the stable input-output dynamics. Furthermore, BPOD models proved to capture these dynamics with less modes, which is in agreement with our previous results on the backward-facing step flow.

It should be mentioned here that the present BPOD procedure based on frequential definitions of the Gramians reduces the stable and unstable subspaces simultaneously.³⁹ In other words, it is equivalent to separating the stable and unstable parts of the transfer function and performing the model reduction for both parts separately. This may explain the quick ability of BPOD ROMs to capture simultaneously and gradually the unstable (see Figures 13(a) and 14(a)) as well as the stable input-output dynamics (see Figure 17(a)).

Concerning POD models, the same idea does not hold and, as a result, their ability to model both dynamics is not as progressive. Indeed, observing Figure 13(b), we note that the modeling of the unstable subspace is not gradual and, most importantly, we show in Figure 17(b) that the POD ROMs are completely unable to model the correct stable dynamics until the unstable subspace is well captured from $r \approx 82$. This latter point may indicate that a bad modeling of the unstable subspace involves the incapability of POD ROMs to correctly model the stable dynamics.

Finally, it should be emphasized that our frequential approach to perform BPOD and POD model reduction is not based on a partition of the unstable and stable subspaces contrary to the previous works on the literature.^{14,15} In their case, they had to (1) compute the global eigenmodes by a

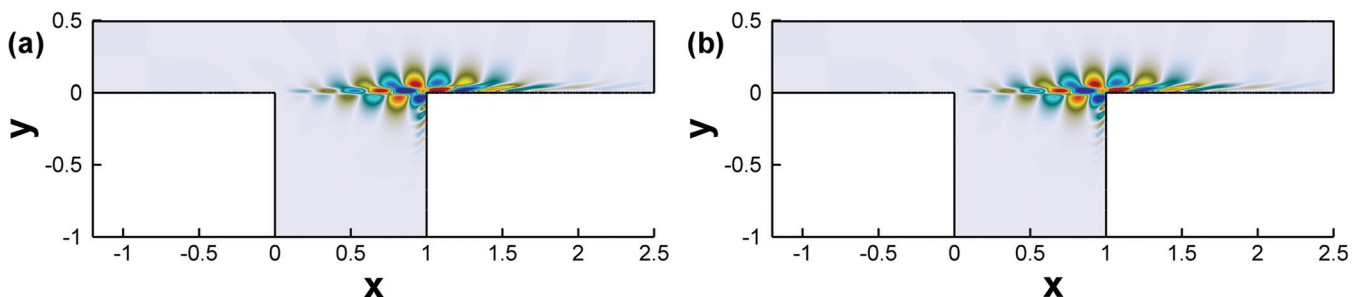


FIG. 15. (Color online) Real part of the longitudinal velocity of the most unstable eigenvector E_{-3} . (a) Solution obtained with the full system with a shift and invert Arnoldi algorithm. (b) Solution obtained with a reduced-order model built with 150 POD modes.

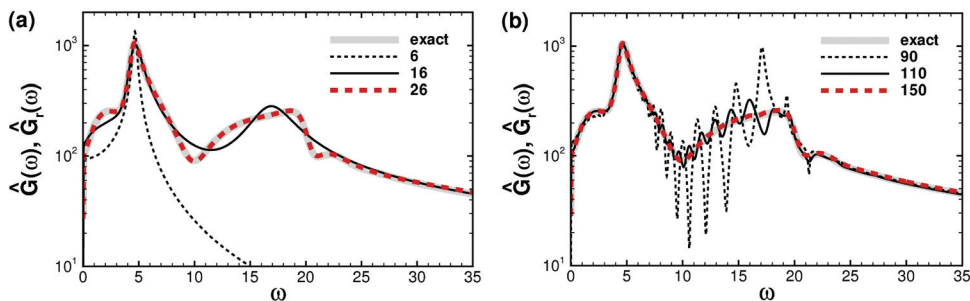


FIG. 16. (Color online) Transfer function of the full system stable part compared to those of (a) BPOD and (b) POD models.

shift and invert Arnoldi algorithm and (2) perform a direct and adjoint time-stepping simulation, while projecting at each time step (with the global modes), the resulting states onto the stable subspace. Their unstable dynamics is then modeled by the unstable global modes while their snapshots arising from the direct and adjoint simulations are used to build BPOD models^{14,15} (and POD models¹⁵) of the stable input-output dynamics. The square cavity flow configuration studied in this section has thus illustrated the ability of the frequential snapshots to build BPOD and POD ROMs of an unstable flow system without separating the unstable and stable subspaces. This proved to be a valuable asset insofar as we neither had to compute any global modes nor to perform any projection onto the stable subspace.

V. CONCLUSION

In this paper, we have described how the use of frequential responses of a flow to a given actuator enables to compute the basis of the most controllable modes (POD modes). Analogously, the harmonic flow states yielding the maximum contribution to the sensor energy have been introduced to compute the most and equally controllable and observable modes: the balanced modes (BPOD modes). ROMs have been designed by the projection of the full original system of equations onto BPOD/POD modes computed from the so-called frequency snapshots.

As a first step, the whole procedure has been carried out on a stable linear system: the flow over a rounded backward-facing step. The first example stands for a well-known noise amplifier flow in the sense that small perturbations can be strongly amplified through the shear layer. The computation of the frequency snapshots highlighted the frequency selection process of the flow. In particular, an energy peak of the flow response to harmonic actuation has been observed

nearby the frequency associated with the Kelvin-Helmholtz instability. These frequential snapshots have then been used to build the BPOD and POD models that proved to be effective in modeling the linear input-output behavior of the flow. Both the impulse response and transfer function are recovered by the ROMs and a better efficiency of BPOD models to do so was observed as expected from the literature.

As a second step, we moved on to the case of a linear unstable system. To assess and quantify the ability of our procedure to reduce unstable systems, we applied the same technique on a well-known oscillator system: the flow over a square cavity. On the one hand, the resulting ROMs were shown to capture the same unstable global modes as those of the original system and, on the other hand, an accurate modeling of the stable dynamics has also been recovered by investigating the stable transfer functions. Similarly, a superiority of BPOD models over POD ones was noticed. Contrary to the reference work on this flow configuration¹⁵ where the authors made a partition to model the stable (using BPOD/POD ROMs based on temporal snapshots) and unstable (using global modes) subspaces separately, our model reduction technique has proved to model efficiently at the same time both dynamics.

In summary, we proved the possibility and efficiency of frequential snapshots to yield BPOD and POD models that are (1) identical to those computed from temporal snapshots for stable systems and (2) operational for unstable systems without separating the unstable and stable subspaces. Therefore, this contribution on model reduction seems to be a promising alternative tool to compute POD modes or to approximate balanced truncation. We hope that the present contribution will somehow aid in the design of frequency-based ROMs in view of building efficient closed-loop flow controllers.

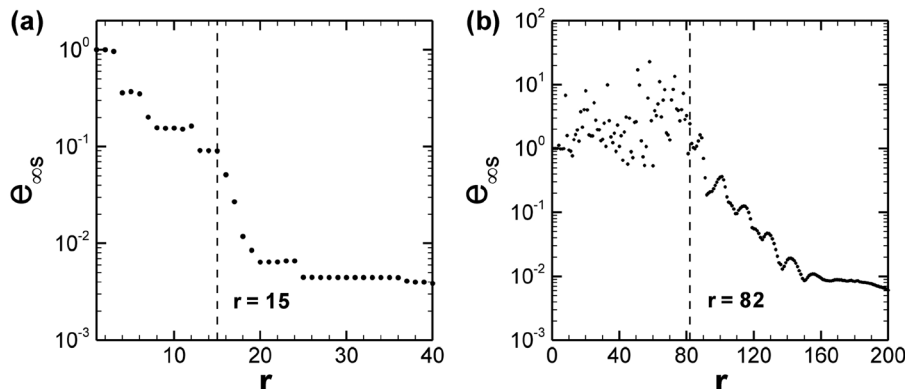


FIG. 17. Relative norm of the error e_{∞} as a function of the size r of the ROMs for (a) the BPOD and (b) the POD models. The limits from which the ROMs exhibit eight unstable global modes are depicted by dashed lines standing for $r = 15$ and $r = 82$ respectively.

ACKNOWLEDGMENTS

The authors gratefully acknowledge the French “Délégation Générale pour l’Armement” (DGA) for financial support.

APPENDIX A: FORMULATION OF THE INCOMPRESSIBLE LINEARIZED NAVIER-STOKES EQUATIONS AS A STANDARD STATE-SPACE SYSTEM

The design of reduced-order models requires to reformulate the linearized Navier-Stokes equations into a standard state-space form. Yet, this is not trivial since the matrix before the time derivative is not invertible because of incompressibility. To this end, we proceed as in Barbagallo *et al.*¹⁵ We first multiply the momentum equation by $A_2 Q_1^{-1}$, which yields, assuming that $A_2 \dot{X}_1 = 0$, an expression for the pressure in terms of the velocity field

$$X_2 = -(A_2 Q_1^{-1} A_2^*)^{-1} [(A_2 Q_1^{-1} A_1) X_1 + A_2 B_1 c(t)]. \quad (A1)$$

This relation can be used to eliminate the explicit divergence constraint and allows us to write the governing linearized equations in the desired form

$$\frac{dX_1}{dt} = P_1 A_1 X_1 + P_1 Q_1 B_1 c(t), \quad (A2a)$$

$$m(t) = C_1 X_1, \quad (A2b)$$

where

$$P_1 Q_1 = I - Q_1^{-1} A_2^* (A_2 Q_1^{-1} A_2^*)^{-1} A_2 \quad (A3)$$

is the projection matrix onto the divergence-free space. It is noteworthy that P_1 is a Hermitian operator, so that we can take advantage of the relation $P_1^* = P_1$. By defining $A = P_1 A_1$, $B = P_1 Q_1 B_1$, and $C = C_1$, we recover Eq. (5).

APPENDIX B: EXPRESSING THE FREQUENTIAL SNAPSHOTS IN RELATION TO THE LINEARIZED NAVIER-STOKES EQUATIONS

1. Direct snapshots

The direct flow states \hat{X}_1 involved in the snapshots method are defined in Eqs. (10). Substituting A and B by their expression calculated in Appendix A leads to

$$(j\omega I - P_1 A_1) \hat{X}_1 = P_1 Q_1 B_1. \quad (B1)$$

If we introduce the pressure \hat{X}_2 associated to \hat{X}_1 by

$$\hat{X}_2 = -(A_2 Q_1^{-1} A_2^*)^{-1} [(A_2 Q_1^{-1} A_1) \hat{X}_1 + A_2 B_1], \quad (B2)$$

we get

$$j\omega \hat{X}_1 - Q_1^{-1} A_1 \hat{X}_1 - Q_1^{-1} A_2^* \hat{X}_2 = B_1 \quad (B3)$$

so that we recover Eq. (16)

$$\left[j\omega \begin{pmatrix} Q_1 & 0 \\ 0 & 0 \end{pmatrix} - \begin{pmatrix} A_1 & A_2^* \\ A_2 & 0 \end{pmatrix} \right] \begin{pmatrix} \hat{X}_1 \\ \hat{X}_2 \end{pmatrix} = \begin{pmatrix} Q_1 & 0 \\ 0 & 0 \end{pmatrix} \begin{pmatrix} B_1 \\ 0 \end{pmatrix}. \quad (B4)$$

The finite number of flow fields $\hat{X}_1(\omega_i)$ at discrete pulsations ω_i can be obtained by inverting this linear system and are stacked as columns of the matrix X_1 . The above demonstration shows that the controllability Gramian G_c , defined in Eq. (14), can be thought of as the spatial correlation matrix for the harmonic responses to harmonic forcings at the actuator location.

2. Adjoint snapshots

The adjoint flow states \hat{Y}_1 involved in the snapshot method are defined in Eqs. (10). In a similar manner, a substitution of the expressions of A and C calculated in Appendix A leads to

$$(-j\omega I - P_1 A_1^*) P_1 Q_1 \hat{Y}_1 = P_1 Q_1 (Q_1^{-1} C_1^*). \quad (B5)$$

If we omit the incompressibility constraint $P_1 Q_1$ on \hat{Y}_1 , which is already applied through the evolution operator $(-j\omega I - P_1 A_1^*)$, we have

$$(-j\omega I - P_1 A_1^*) \hat{Y}_1 = P_1 Q_1 (Q_1^{-1} C_1^*). \quad (B6)$$

Similarly, if we introduce the adjoint pressure \hat{Y}_2 associated to \hat{Y}_1 by

$$\hat{Y}_2 = -(A_2 Q_1^{-1} A_2^*)^{-1} [(A_2 Q_1^{-1} A_1^*) \hat{Y}_1 + A_2 Q_1^{-1} C_1^*] \quad (B7)$$

we get

$$-j\omega \hat{Y}_1 - Q_1^{-1} A_1^* \hat{Y}_1 - Q_1^{-1} A_2^* \hat{Y}_2 = Q_1^{-1} C_1^* \quad (B8)$$

so that we recover Eq. (17)

$$\left[-j\omega \begin{pmatrix} Q_1 & 0 \\ 0 & 0 \end{pmatrix} - \begin{pmatrix} A_1^* & A_2^* \\ A_2 & 0 \end{pmatrix} \right] \begin{pmatrix} \hat{Y}_1 \\ \hat{Y}_2 \end{pmatrix} = \begin{pmatrix} C_1^* \\ 0 \end{pmatrix}. \quad (B9)$$

The finite number of flow fields $\hat{Y}_1(\omega_i)$ at discrete pulsations ω_i can be obtained by inverting this linear system and are stacked as columns of the matrix Y_1 . Analogously, The observability Gramian G_o can be thought of as the spatial correlation matrix for the harmonic responses of the adjoint system to harmonic forcings at the sensor location.

APPENDIX C: EIGENSPECTRUM OF POD MODELS

This appendix is devoted to showing an interesting observation on the eigenspectrum of POD models. We have represented in Figure 18(a) a larger part of the eigenspectrum corresponding to models of size $r=120$, $r=140$, and $r=200$ together with the spectrum of global eigenmodes (taken from the work of Barbagallo *et al.*¹⁵). As detailed in Sec. IV, the unstable eigenvalues of POD models tend to

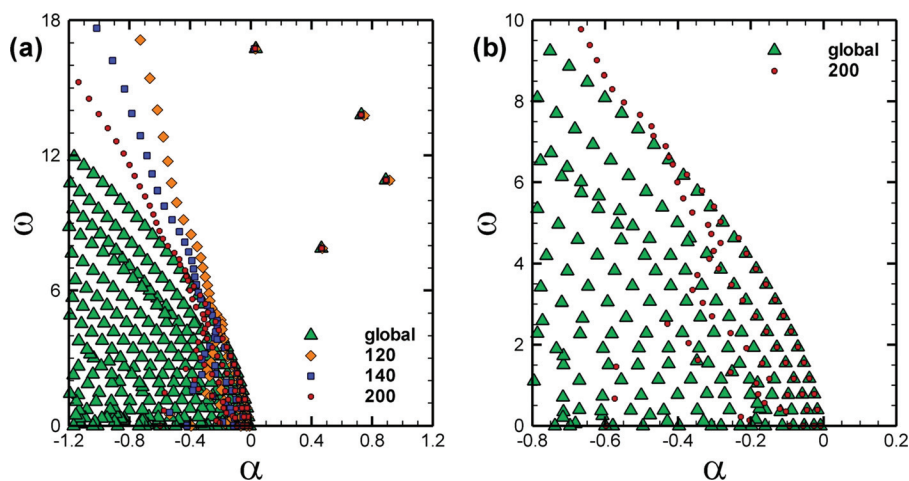


FIG. 18. (Color online) (a) Part of the eigenspectrum of POD models of size 120, 140, and 200 superimposed onto that of the full system. A closer view is depicted for the model of size 200 on (b).

those of the full system. Here, we take a closer look at the stable part of the eigenspectrum ($\alpha < 0$). The global eigenspectrum, depicted by triangles, is characterized by eigenmodes organized in branches. We notice that each POD eigenspectrum displays a branch of modes that tends to the most unstable branch of the global eigenspectrum as the model size r is increased.

Figure 18(b) represents the same global eigenspectrum focused on the region $-0.8 < \alpha < 0.2$ and that of a POD model of size 200. It is strikingly noticed that the first unstable POD eigenvalues superimpose onto the first global eigenmodes. Note that BPOD models do not yield the same observation (not shown here). This result suggests that the POD procedure somehow rebuilds the original spectrum of the original full system.

¹J. Kim and T. Bewley, "A linear systems approach to flow control," *Annu. Rev. Fluid Mech.* **39**, 383 (2007).

²D. Sipp, O. Marquet, P. Meliga, and A. Barbagallo, "Dynamics and control of global instabilities in open flows: A linearized approach," *Appl. Mech. Rev.* **63**, 030801 (2010).

³T. R. Bewley and S. Liu, "Optimal and robust control and estimation of linear paths to transition," *J. Fluid Mech.* **365**, 305 (1998).

⁴T. R. Bewley, "Flow control: New challenges for a new renaissance," *Prog. Aerosp. Sci.* **37**, 21 (2001).

⁵J. B. Burl, *Linear Optimal Control: \mathcal{H}_2 and \mathcal{H}_∞ Methods* (Addison Wesley Longman, Inc., Menlo Park, CA, 1999).

⁶K. Zhou, G. Salomon, and E. Wu, *Robust and Optimal Control* (Prentice-Hall, New Jersey, 2002).

⁷M. Högberg, and D. S. Henningson, "Linear optimal control applied to instabilities in spatially developing boundary layers," *J. Fluid Mech.* **470**, 151 (2002).

⁸M. Chevalier, J. Høpfner, E. Åkervik, and D. Henningson, "Linear feedback control and estimation applied to instabilities in spatially developing boundary layers," *J. Fluid Mech.* **588**, 163 (2007).

⁹M. Högberg, T. R. Bewley, and D. S. Henningson, "Linear feedback control and estimation of transition in plane channel flow," *J. Fluid Mech.* **481**, 149 (2003).

¹⁰P. Moin and T. Bewley, "Feedback control of turbulence," *Appl. Mech. Rev.* **47**, 3 (1994).

¹¹S. Joshi, J. Speyer, and J. Kim, "A systems theory approach to the feedback stabilization of infinitesimal and finite-amplitude disturbances in plane Poiseuille flow," *J. Fluid Mech.* **332**, 157 (1997).

¹²E. Åkervik, J. Høpfner, U. Ehrenstein, and D. S. Henningson, "Optimal growth, model reduction and control in a separated boundary-layer flow using global modes," *J. Fluid Mech.* **579**, 305 (2007).

¹³S. Bagheri, L. Brandt, and D. S. Henningson, "Input-output analysis, model reduction and control of the flat-plate boundary layer," *J. Fluid Mech.* **620**, 263 (2009).

¹⁴S. Ahuja and C. Rowley, "Feedback control of unstable steady states of flow past a flat plate using reduced-order estimators," *J. Fluid Mech.* **645**, 447 (2010).

¹⁵A. Barbagallo, D. Sipp, and P. Schmid, "Closed-loop control of an open cavity flow using reduced-order models," *J. Fluid Mech.* **641**, 1 (2009).

¹⁶J. L. Lumley, *Stochastic Tools in Turbulence* (Academic, New York, 1970).

¹⁷L. Sirovich, "Turbulence and the dynamics of coherent structures," *Q. Appl. Math.* **45**, 561 (1987).

¹⁸G. Berkooz, P. Holmes, and J. L. Lumley, "The proper orthogonal decomposition in the analysis of turbulent flows," *Annu. Rev. Fluid Mech.* **25**, 539 (1993).

¹⁹N. Aubry, P. Holmes, J. L. Lumley, and E. Stone, "The dynamics of coherent structures in the wall region of a turbulent boundary layer," *J. Fluid Mech.* **192**, 115 (1988).

²⁰N. Aubry, R. Guyonnet, and R. Lima, "Spatio-temporal analysis of complex signals: Theory and applications," *J. Stat. Phys.* **64**, 683 (1991).

²¹B. Noack, K. Afanasiev, M. Morzynski, G. Tadmor, and F. Thiele, "A hierarchy of low-dimensional models for the transient and post-transient cylinder wake," *J. Fluid Mech.* **497**, 335 (2003).

²²M. Buffoni, S. Camarri, and A. Iollo, "Low-dimensional modelling of a confined three-dimensional wake flow," *J. Fluid Mech.* **569**, 141 (2006).

²³B. Galletti, A. Bottaro, C. Bruneau, and A. Iollo, "Accurate model reduction of transient and forced wakes," *Eur. J. Mech. B/Fluids* **26**, 354 (2007).

²⁴J. Delville, L. Cordier, and J. Bonnet, "Large-scale structure identification and control in turbulent shear flows," in *Flow Control: Fundamentals and Practice* (Springer-Verlag, Berlin, 1998), pp. 199–273.

²⁵G. Tadmor, B. Noack, M. Morzynski, and S. Siegel, "Low-dimensional models for feedback flow control. Part II. Control design and dynamical estimation," AIAA Paper 2004-2409, 2004.

²⁶M. Bergmann, L. Cordier, and J.-P. Brancher, "Optimal rotary control of the cylinder wake using pod reduced-order model," *Phys. Fluids* **17**, 305 (2005).

²⁷M. Samimy, M. Debiasi, E. Caraballo, A. Serrani, X. Yuan, J. Little, and J. Myatt, "Feedback control of subsonic cavity flows using reduced-order models," *J. Fluid Mech.* **579**, 315 (2007).

²⁸C. Rowley, T. Colonius, and R. Murray, "Model reduction for compressible flows using pod and Galerkin projection," *Physica D* **189**, 115 (2004).

²⁹B. Moore, "Principal component analysis in linear systems: Controllability, observability, and model reduction," *IEEE Trans. Autom. Control* **26**, 17 (1981).

³⁰J. M. Scherpen, "Balancing for nonlinear systems," *Syst. Control Lett.* **21**, 143 (1993).

³¹S. Lall, J. E. Marsden, and S. Glavaski, "A subspace approach to balanced truncation for model reduction of nonlinear control systems," *Int. J. Robust Nonlinear Control* **12**, 519 (2002).

³²A. Laub, M. Heath, C. Paige, and R. Ward, "Computation of system balancing transformations and other applications of simultaneous diagonalization algorithms," *IEEE Trans. Autom. Control* **32**, 115 (1987).

³³L. Cortezzi and J. Speyer, "Robust reduced-order controller of laminar boundary layer transitions," *Phys. Rev. E* **58**, 1906 (1998).

- ³⁴K. Willcox and J. Peraire, "Balanced model reduction via proper orthogonal decomposition," *AIAA J.* **40**, 2323 (2002).
- ³⁵C. Rowley, "Model reduction for fluids using balanced proper orthogonal decomposition," *Int. J. Bifurcation Chaos Appl. Sci. Eng.* **15**, 997 (2005).
- ³⁶M. Ilak and C. Rowley, "Reduced-order modeling of channel flow using travelling POD and balanced POD," AIAA Paper 2006-3194, 3rd AIAA Flow Control Conference, 2006.
- ³⁷M. Ilak and C. Rowley, "Modeling of transitional channel flow using balanced proper orthogonal decomposition," *Phys. Fluids* **20**, 034103 (2008).
- ³⁸S. Bagheri, J. Høpfner, P. J. Schmid, and D. S. Henningson, "Input-output analysis and control design applied to a linear model of spatially developing flows," *Appl. Mech. Rev.* **62**, 020803 (2009).
- ³⁹K. Zhou, G. Salomon, and E. Wu, "Balanced realization and model reduction for unstable systems," *Int. J. Robust Nonlinear Control* **9**, 183 (1999).
- ⁴⁰T. Kim, "Frequency-domain Karhunen-Loeve method and its application to linear dynamic systems," *AIAA J.* **36**, 2117 (1998).
- ⁴¹A. C. Antoulas, *Approximation of Large-Scale Dynamical Systems* (SIAM, Philadelphia, 2005).
- ⁴²S. Ahuja and C. Rowley, "Low-dimensional models for feedback stabilization of unstable steady states," AIAA Paper 2008-553, 46th AIAA Aerospace Sciences Meeting and Exhibit, 2008.
- ⁴³C. W. Rowley, I. Mezić, S. Bagheri, P. Schlatter, and D. S. Henningson, "Spectral analysis of nonlinear flows," *J. Fluid Mech.* **641**, 115 (2009).
- ⁴⁴P. J. Schmid, "Dynamic mode decomposition of numerical and experimental data," *J. Fluid Mech.* **656**, 5 (2010).
- ⁴⁵B. R. Noack, P. Papas, and P. A. Monkewitz, "The need for a pressure-term representation in empirical galerkin models of incompressible shear flow," *J. Fluid Mech.* **523**, 339 (2005).
- ⁴⁶A. C. Or and J. L. Speyer, "Model reduction of input-output dynamical systems by proper orthogonal decomposition," *J. Guid. Control Dyn.* **31-2**, 322 (2008).
- ⁴⁷Z. Ma, S. Ahuja, and C. W. Rowley, "Reduced order models for control of fluids using the eigensystem realization algorithm," *Theor. Comput. Fluid Dyn.* (2010).
- ⁴⁸O. Marquet and D. Sipp, "Global sustained perturbations in a backward-facing step flow," in *Proceedings of the 7th IUTAM Symposium on Laminar-Turbulent Transition*, edited by P. Schlatter and D. S. Henningson, IUTAM (Springer, Dordrecht, the Netherlands, 2009), pp. 525–528.
- ⁴⁹P. R. Amestoy, I. S. Duff, J. Koster, and J.-Y. L'Excellent, "A fully asynchronous multifrontal solver using distributed dynamic scheduling," *SIAM J. Matrix Anal. Appl.* **23**, 15 (2001).
- ⁵⁰A. Monokrousos, E. Åkervik, L. Brandt, and D. S. Henningson, "Global three-dimensional optimal disturbances in the Blasius boundary-layer flow using time-steppers," *J. Fluid Mech.* **650**, 181 (2010).
- ⁵¹T. Duriez, "Application des générateurs de vortex au contrôle d'écoulements décollés," Ph.D. thesis (Paris Diderot University, France, 2009).
- ⁵²D. Sipp and A. Lebedev, "Global stability of base and mean flows: A general approach and its applications to cylinder and open cavity flows," *J. Fluid Mech.* **593**, 333 (2007).
- ⁵³N. Aubry, R. Guyonnet, and R. Lima, "Spatio-temporal symmetries and bifurcations via bi-orthogonal decompositions," *J. Nonlinear Sci.* **2**, 183 (1992).
- ⁵⁴N. Aubry and R. Lima, "The dynamics of spatio-temporal modulations," *Chaos* **5**, 5788 (1995).
- ⁵⁵N. Aubry, R. Lima, and M. Rahibe, "Breaking of space-time symmetries in modulated traveling waves," *Chaos* **13**, 541 (2003).